Interaction of Underwater Blasts and Submerged Structures

S. Abrate

Abstract This chapter examines the interaction of shock waves generated by underwater explosions and submerged structures. Cylindrical shells filled with air, water, or a liquid with a different speed of sound are considered and the specific issue considered is the prediction of the position of the various wave fronts as a function of time. This is a challenging problem for both analytical and numerical approaches due to the sharp discontinuities, the complex shapes of these wave fronts and their numbers. A simple ray tracing procedure is developed to predict the exact position of all the wave fronts. It provides great insight into the physics of the problem and explains the evolution of the shape of the various fronts and the formation of singularities. Applications to the medical field are also presented.

Keywords Underwater blast • Explosion bubble • Shock wave • Wave front • Diffraction

1 Introduction

This chapter deals with the effect of underwater explosions on submerged marine structures and more specifically with the interaction of blast wave with those structures. Underwater explosions have been studied for a long time and much of what is known about the physics of the problem is summarized in a book published by Cole [1] in 1948. These explosions generate a shock wave that propagate through the water at the speed of sound and a large gas bubble that oscillates and migrates towards the free surface. With nearby explosions, a structure will be subjected to both effects and the interaction can be quite complex. As a rule of thumb, if the

S. Abrate (✉)
Department of Mechanical Engineering and Energy Processes, Southern Illinois University, Carbondale, IL 62901-6603, USA
e-mail: abrate@engr.siu.edu

S. Abrate et al. (eds.), *Dynamic Failure of Composite and Sandwich Structures*,
Solid Mechanics and Its Applications 192, DOI 10.1007/978-94-007-5329-7_3,

distance between the bubble and the structure is always larger than three times the maximum radius of the bubble, their interaction can be neglected. Then, the structure is subjected to the effect of the shock wave only.

The next section will review some basic knowledge about underwater explosions and empirical equations used to predict the pressure pulse generated at a point given the mass of the explosive charge and the stand-off distance. The same data can be used to predict the size of the explosion bubble, its frequency of oscillation, and how fast it migrates towards the surface. Some charts are presented to show the effects of the governing parameters and show the order of magnitudes of the quantities predicted by these equations. Section 3 introduces the propagation of waves in solids, liquids, and their interfaces. It covers body waves, surface waves such as Rayleigh waves, Scholte-Stoneley waves, Franz waves, and wave propagation in wave guides as described by the Rayleigh-Lamb theory and various beam, plate and shell theories. Section 4 describes the interaction of between shock waves and submerged structures on a short time scale and on a longer time scale. It shows how shock waves can excite waves propagating along the interface with the water, how it can lead to cavitation, and how the wave is transmitted to the inside of a fluid-filled shell.

Many studies present analytical and numerical approaches for predicting the interaction of a shock wave with submerged cylindrical or spherical shells. While these approaches can generate the response at any point in the fluid or on the surface of the shell, previous studies typically presented plots of pressure versus time or transverse velocity versus time at only a few points around the circumference of the shell. It is then difficult to understand the physics of the problem. Recently, some investigators presented results showing the complex interaction between the shock wave and the structure with many wave fronts that travel, change shape, and sometimes exhibit singularities. Obtaining accurate results numerically for the entire domain is a challenging task and the interpretation of those results can be difficult. Section 5 presents a brief overview of the literature and a simple geometrical approach based on ray tracing for predicting the position of all wave fronts at any given time. It is particularly useful in predicting the shape of certain wave fronts as singularities occur on ray caustics. It also provides valuable insight in cases of liquid-filled shells and particularly when the speed of sound inside in different than that in the outside fluid.

Section 6 shows how the approach developed here can be applied to the analysis of two problems in the medical field: (1) Shock Wave Lithotripsy (SWL) a noninvasive procedure for kidney stone removal; (2) Traumatic Brain Injury (TBI) caused by impact and blast loading.

2 Underwater Explosion in an Infinite Domain

Underwater water explosions generate both a shock wave that decays rapidly with time and an oscillating and migrating explosion bubble (Fig. 1). As the charge is detonated, a pressure pulse is generated. The rise time is very short and it decays

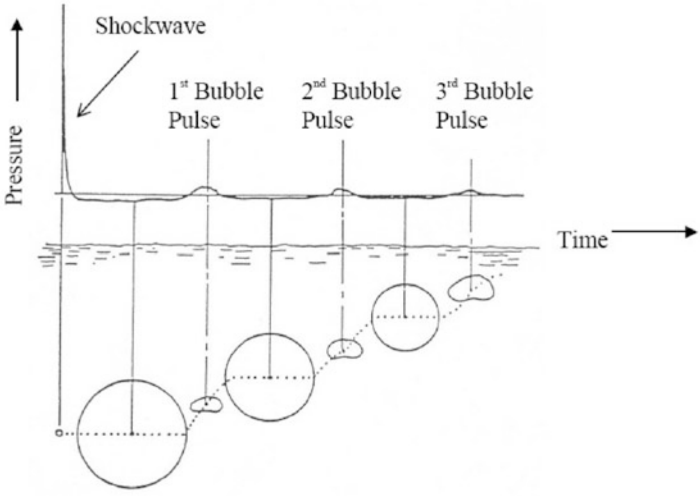

Fig. 1 Shockwave and bubble generated by an underwater blast

rapidly. The pressure wave is called a shock wave because, for high explosives, the pressure raises almost instantly to a maximum pressure at the wave front. This is in contrast with other cases of explosions where the pressure has a finite rise time like the pressure wave generated by the failure of a pressure vessel. This shock wave propagates at the speed of sound over long distances and can cause damage to structural panels but, generally, it does not transfer enough momentum to induce overall deformation of the ship.

Pritchett [2] describes the formation of an explosion bubble for an uncased spherical charge of conventional high explosive such as TNT initiated at the center. As the detonation front expands through the charge, the explosive material it goes through undergoes a chemical reaction and releases energy. The detonation wave speed is typically in the 6,000–7,000 m/s range. As it reaches the surface of the charge and proceeds into the water, the chemical reaction is complete and Y, the total energy released by the explosion, is proportional to the product of Q, the mass of the charge, and q, the energy released per unit mass of the explosive. For TNT, $q = 4.2 \times 10^6$ J/kg. Initially, about half of the energy is contained in the shockwave propagating in the water and the other half is in the gas bubble as kinetic energy and heat. Near the original charge, the nonlinear shock dissipates energy in the water in the form of heat. After the shock wave has travelled 10–15 radii from the origin, this dissipation process is over. Hunter and Gears [3] give a simple rule to estimate the size of the near field where the wave front propagates at speeds that are substantially higher than the acoustic wave propagation. The size of the near field should be twice the maximum radius of the bubble which is approximately 15 times the radius of the charge. Therefore, acoustic wave propagation speed near 1,500 m/s occurs beyond 30 charge radii.

Figure 1 shows the evolution of the pressure in time in which we note a first pulse due to the passage of the shockwave and a series of smaller pulses due to the periodic collapse of the explosion bubble. This figure also shows that the bubble radius periodically reaches a maximum and shrinks or collapses to a minimum while migrating towards the water surface. The migration appears to stop while the bubble radius reaches a maximum and restart once it starts shrinking again. Explosion bubbles oscillate with very low frequencies and can induce whipping of nearby structures and induce severe damage.

2.1 Scaling of Underwater Explosions

Over the years many experimental studies have been conducted over the years and empirical formulas have been developed to characterize the evolution of the free-field pressure behind the shock wave in terms of the mass of the explosive charge and the stand-off distance. Formulas are also available for prediction the evolution of the explosion bubble. The formulas discussed in this section are called scaling equations or similitude equations.

2.1.1 Scaling of the Shock Wave

Following the arrival of the shock wave, the pressure p at a given point decreases exponentially

$$p(t) = p_o e^{-t/t_o} \tag{1}$$

Analysis of experimental results [4] show that the maximum pressure p_o and the characteristic time t_o depend on the ratio $Q^{1/3}/R$ where Q is the mass of the explosive charge and R is distance R from the explosion (also called the stand-off distance). Following Cole [1],

$$p_o = K_1 \left(\frac{Q^{1/3}}{R} \right)^{A_1}, \quad t_o = K_2 Q^{1/3} \left(\frac{Q^{1/3}}{R} \right)^{A_2} \tag{2}$$

where Q is expressed in kg, R in m, p_o in MPa and t_o in ms. K_1, K_2, A_1, and A_2 are constants obtained from experiments. For trinitrotoluene (TNT), these constants are $K_1 = 52.4$, $A_1 = 1.18$, $K_2 = 0.084$, $A_2 = -0.23$. The experiments of Murata et al. [5] indicate that the pressure in both the initial pressure pulse and the bubble pulse follow Eq. (2). As the stand-off distance increases, the maximum pressure p_o decreases (Fig. 2) and the time t_d increases (Fig. 3). Both p_o and t_d increase when Q, the mass of the charge, increases.

Many other expressions are available for scaling of underwater explosions. The mass of the explosive can be written as $Q = (4/3)\pi \rho_E a^3$ where ρ_E is the density of the explosive and a is the equivalent spherical radius of the charge. Then, the term

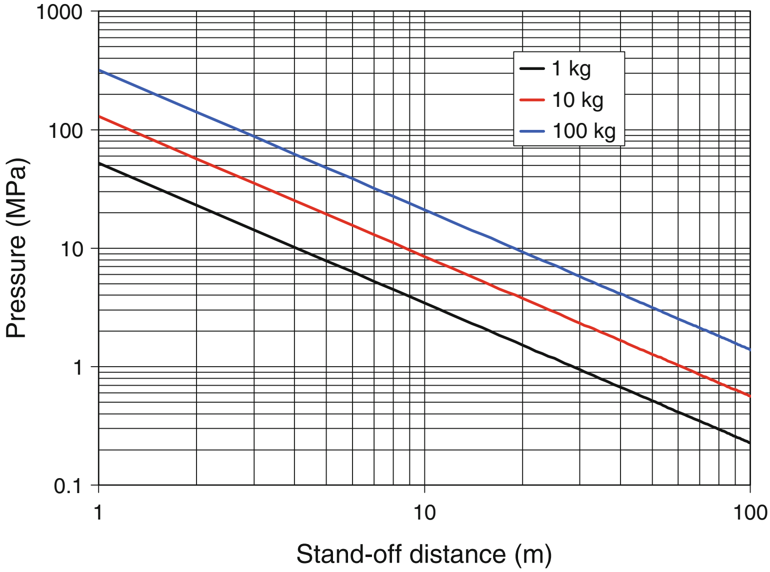

Fig. 2 Maximum pressure during underwater explosion as a function of standoff distance and mass of the charge

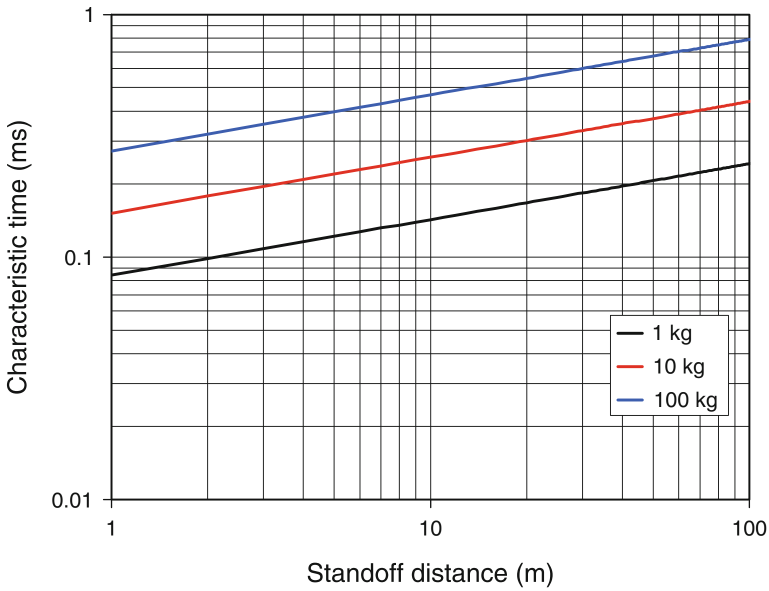

Fig. 3 Characteristic time for underwater explosion as a function of standoff distance and mass of the charge

$Q^{1/3}/R$ in Eq. (2) is proportional to a/R, the ratio of the radius of the charge and the stand-off distance. Some authors write Eq. (2) in terms of a/R. In Refs. [37, 38] Eq. (1) is written as

$$p = P_c\,[a/R]^{1/A}\,f(\tau) \tag{3}$$

in terms $\tau = \nu_c\,(a/R)^B\,t/a$ and four constants P_c, ν_c, A, and B. It can be shown that τ in this expression is equal to t/t_o in Eq. (1). Then, the function $f(\tau)$ is taken to be

$$f(\tau) = e^{-\tau} \qquad \text{when} \quad \tau \le 1 \tag{4}$$

and

$$f(\tau) = 0.8251\,e^{-1.338\,\tau} + 0.1749\,e^{-0.1805\,\tau} \qquad \text{when} \qquad 1 < \tau \le 7 \tag{5}$$

Combining Eqs. (3) and (4), we recover Eq. (1) which is said to be valid until the end of the expansion phase of bubble ($\tau = 1$). Equation (5) covers the oscillation phase of the bubble. Equations. (3, 4 and 5) were used by Kalavalapally et al. [6, 7]. Van der Schaaf [8] found that the pressure varies according to Eqs. (1) and (2) when $t < t_o$ but observed a decay slower than exponential at larger times. The pressure was approximated by

$$p(t) = \begin{cases} p_o e^{-t/t_o} & \text{for} \quad t \le t_o \\ p_o t_o \,/\, (t.e) & \text{for } t_o \le t \le nt_o \;\; p_o e^{-t/t_o} \\ 0 & \text{for} \quad t > nt_o \end{cases} \tag{6}$$

with n between 5 and 10.

Empirical Eqs. (1 and 2) are widely used to predict the main characteristics of the shock wave generated by underwater explosions. A few new studies serve as reminders that the expressions are used to fit experimental results and slight improvements are always possible. Figures 1, 2 and 3 give general trends and orders of magnitudes for the maximum pressures and characteristic times.

2.1.2 Scaling of the Explosion Bubble

The bubble consists of high-pressure, high-temperature gases generated by the explosion that initially expands. Because of inertia, the bubble over-expands, the pressure inside the bubble becomes less than that of the surrounding water and it collapses. Similarly, as the bubble shrinks, the pressure inside eventually becomes larger than the pressure outside and the bubble will expand again. This new expansion will generate a new but less severe shock wave. This oscillation cycle repeats several times but decays rapidly. In addition, the bubble tends to move up

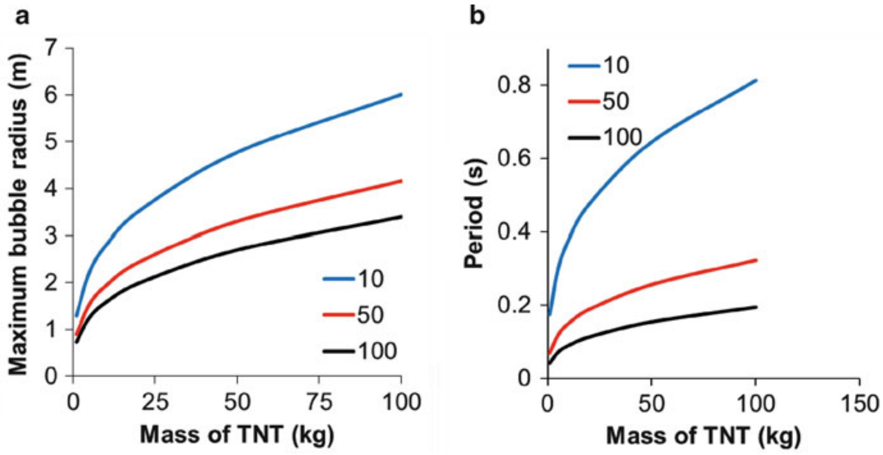

Fig. 4 Oscillating explosion bubble as a function of the explosive charge for three values of the charge depth: 10, 50, 100 m. (**a**) Maximum radius; (**b**) Period of the first bubble oscillation

towards the surface. Bubble pulsations can lead to significant pressure impulses on nearby ship hulls. The maximum bubble radius and the first bubble oscillation period are given by

$$R_{max} = K_3 \ (Q/Z_o)^{1/3} \tag{7}$$

and

$$T = K_4 \ \left(Q^{1/3}/Z_o^{5/6}\right) \tag{8}$$

where $Z_0 = D + 9.8$ is the total static pressure at the location of the explosive, $K_3 = 3.50$ and $K_4 = 2.11$ (Reid [9]). Equation (8) was obtained by curve fitting of experimental results by Arons et al. [10] who examined the periods of the first eight oscillations of the gas bubble. A different constant K_4 was given for each period. Chapman [11] validated Eq. (8) with $Z_0 = D + 10.1$ for $80 < Z < 6{,}700$ m. In several references [12–14] the maximum radius is calculated using (Fig. 4)

$$R_{max} = 3.38 \left(\frac{Q}{D + 10}\right)^{1/3} \tag{9}$$

In the example taken from Vernon [15], with a 227 kg charge of TNT at 45 m, Eq. (2) predicts that $p_o = 4.957$ MPa and $t_o = 0.811$ ms. Equations (7, 8) predict a maximum bubble radius $R_{max} = 5.62$ m and a first oscillation period $T = 0.458$ s while with Eq. (9) the maximum radius is slightly different: $R_{max} = 5.42$ m. The period of the oscillation bubble is in good agreement with Vernon's results. The period of the oscillation bubble (0.458 s) is much larger than the characteristic time of the shock wave (0.811 ms).

Equations (7, 8) give the period and maximum radius of the explosion bubble for its first oscillation. Snay [16] extended these formulas to give the period and maximum radii for all subsequent oscillations. Leybourne [17] suggested that the bubble oscillations period should vary according to

$$T_i = K_4 \left(Q^{1/3}/Z_o^{5/6}\right)/i^{1/2} \tag{10}$$

Pulsation periods are often close to bending frequencies of ships and can cause large amplitude heave and whipping motion. Vernon [15] showed how to determine the far-field acceleration of the fluid, the forces acting on the ship, and the ship's response. When the gas bubble is close to a submarine or a ship hull, this bubble may collapse onto the hull and produce a high speed water jet with water velocities of 130–170 m/s [18].

For TNT, the migration of the gas bubble between the location of the explosive to the location at the time of the first minimum bubble radius is given by [18]

$$m = \frac{12.2}{D + 9.8} Q^{1/2} \tag{11}$$

For 1,000 kg TNT charge at a depth of 60 m, the bubble moves up by 6.24 m during the first bubble oscillation. The ratio between the initial radius R_o and the maximum bubble radius R_m is given empirically by [13]

$$R_o/R_m = 0.0327\,D^{1/3} \tag{12}$$

Relationships between energy, period and maximum radii for two consecutive cycles [19]

$$\frac{E_{n+1}}{E_n} = \left(\frac{T_{n+1}}{T_n}\right)^3 = \left(\frac{R_{m,n+1}}{R_{m,n}}\right)^3 \tag{13}$$

where E is the sum of the potential energy and the kinetic energy of the system. Typically, T_2/T_1 and $R_{m,2}/R_{m,1}$ are approximately equal to 0.70.

2.2 Oscillations of the Explosion Bubble

The period of oscillations can be estimated using a formula attributed to Rayleigh [19, 20] or Willis [21, 22]

$$T = 1.83\,R_{max}\left(\frac{\rho}{p_\infty - p_v}\right)^{1/2} \tag{14}$$

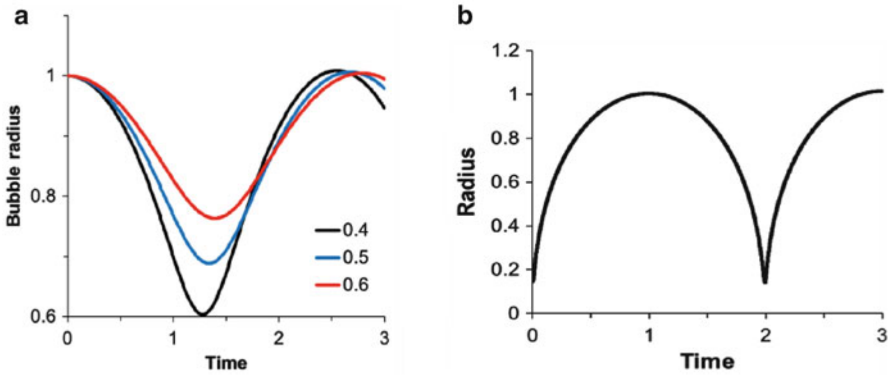

Fig. 5 (**a**) Non-dimensional bubble radius versus non-dimensional time for three values of the parameter ε and $\gamma = 4/3$; (**b**) Oscillations of an explosion bubble with $\varepsilon = 103.36$, $\gamma = 1.25$ and $\xi_0 = 0.1467$

where $p_\infty = p_{ATM} + \rho g h$ is the reference pressure at the hydrostatic depth h far away from the bubble, p_{ATM} is the atmospheric pressure (1 bar), g the acceleration due to gravity and ρ is the fluid density. The vapor pressure p_v is a function of the temperature of the bubble wall only and is assumed to be small ($p_v \sim 2$ kPa at 20°C) and is often neglected [19]. Equation (15) is consistent with Eq. (8) since from Eq. (7), $(Q/Z_0)^{1/3} = R_{max}/K_3$ and after substitution into Eq. (8), $T = \frac{K_4}{K_3}\frac{R_{max}}{Z_o^{1/2}}$. Neglecting p_v, $p_\infty = \rho g Z_0$ and finally, $T = \sqrt{g}\frac{K_4}{K_3} R_{max}(\rho/p_\infty)^{1/2}$. Using the values of K_3 and K_4 given above and $g = 9.81$ m/s^2, gives $\sqrt{g}\,K_4/K_3 = 1.888$.

First derived by Lamb [23] and usually attributed to Rayleigh [20], the Rayleigh-Plesset equation governing the oscillation of spherical bubbles is

$$\ddot{\xi}\xi + 1.5\,\dot{\xi}^2 - \varepsilon\,(\xi_o/\xi)^{3\gamma} + 1 = 0 \tag{15}$$

where $\xi = R/R_{max}$ is the dimensionless radius of the bubble and ξ_0 is its initial value. The parameter ε is the ratio between p_b, the initial pressure inside the bubble, and $p_\infty - p_v$. Integrating Eq. (15) numerically for $\gamma = 4/3$ and $\varepsilon = 0.4$, 0.5 and 0.6, the results shown in Fig. 5a show that the radius decreases progressively until it a minimum value is reached at time T/2 and then bounces back. This example taken from Ref. [24], shows the typical behavior for a cavitation bubble for which ε is small. Lee et al. [19] considered an explosion bubble with much higher value of ε. For that case, the results in Fig. 5b indicate that the bubble collapses abruptly at the end of the first cycle. Afanasiev and Grigorieva [24] used the following approximate relation for the minimum non-dimensional radius

$$R'_{min} \approx \frac{3\varepsilon}{1 + 3\varepsilon - \varepsilon^{3/2}} \tag{16}$$

Extensive research on the oscillation of bubbles in a liquid have considered various complicating factors: (1) bubbles are not necessarily spherical and do not remain spherical as they collapse [25–27]; (2) the Rayleigh-Plesset model predicts undamped oscillation of the gas bubble because the surrounding fluid was assumed to be incompressible [28] and, assuming that surrounding water is governed by the wave equation [29] damping of the bubble oscillations was predicted and excellent agreement with experimental results was obtained [28]; (3) with a model accounting for the effects of the pressure inside the bubble, the water depth, and the compressibility of the surrounding fluid [30], the empirical relations for the maximum bubble radius and the bubble collapse time (Eqs. 7 and 8) are recovered.

2.3 Other Types of Explosives

The preceding equations were developed for TNT explosions. For other types of explosives, it is possible to use the same equations after calculating the equivalent TNT charge Q_{TNT} as follows

$$Q_{TNT} = Q_{exp} H_{exp} / H_{TNT} \tag{17}$$

where Q_{exp} is the mass of the explosive used, H_{TNT} is the heat of detonation of TNT, and H_{exp} is the heat of detonation of the explosive used [31]. $H_{TNT} = 4.520 \times 10^3$ kJ/kg [32].

3 Wave Propagation in Solids and Fluids

Wave propagation in elastic solids is treated in details in several books [33–36]. Brekhovskikh [37] describes the propagation of waves in layered media. Viktorov [38] focused on Rayleigh and Lamb waves. Lighthill [39] and Whitham [40] discuss waves in fluid and Brekhovskikh and Lysanov [41] cover the more specialized topic of ocean acoustics. This section discusses wave propagation in bulk solids, along the surface of a solid, and along the interface between a solid and a liquid. Finally, some basic results concerning propagation of elastic waves in elastic layers and the connection between elasticity theory and plate theories are presented.

3.1 Wave Propagation in Unbounded Solids

The equations of motion for an elastic solid are

$$\sigma_{ji,j} = \rho \ddot{u}_i \tag{18}$$

in terms of the stress components σ_{ij} and the displacement u_i. For an orthotropic material, the stress strain relations can be written as

$$\begin{Bmatrix} \sigma_{11} \\ \sigma_{22} \\ \sigma_{33} \\ \sigma_{23} \\ \sigma_{31} \\ \sigma_{12} \end{Bmatrix} = \begin{bmatrix} C_{11} & C_{12} & C_{13} & 0 & 0 & 0 \\ C_{12} & C_{22} & C_{23} & 0 & 0 & 0 \\ C_{13} & C_{23} & C_{33} & 0 & 0 & 0 \\ 0 & 0 & 0 & C_{44} & 0 & 0 \\ 0 & 0 & 0 & 0 & C_{55} & 0 \\ 0 & 0 & 0 & 0 & 0 & C_{66} \end{bmatrix} \begin{Bmatrix} \varepsilon_{11} \\ \varepsilon_{22} \\ \varepsilon_{33} \\ \varepsilon_{23} \\ \varepsilon_{31} \\ \varepsilon_{12} \end{Bmatrix} \tag{19}$$

in material principal coordinates. The strain–displacement relations are

$$\begin{aligned} &\varepsilon_{11} = u_{1,1}, \quad \varepsilon_{22} = u_{2,2}, \quad \varepsilon_{33} = u_{3,3}, \\ &\varepsilon_{23} = u_{2,3} + u_{3,2}, \quad \varepsilon_{31} = u_{3,1} + u_{1,3}, \quad \varepsilon_{12} = u_{1,2} + u_{2,1} \end{aligned} \tag{20}$$

The material behavior is defined by three elastic moduli (E_1, E_2, and E_3), three shear moduli (G_{12}, G_{13}, and G_{23}), and three Poisson's ratios (ν_{12}, ν_{13}, and ν_{23}). With these nine parameters, the stiffness coefficients are

$$C_{11} = E_1 (1 - \nu_{23}\nu_{32}) / \Delta, \quad C_{22} = E_2 (1 - \nu_{31}\nu_{13}) / \Delta, \quad C_{33} = E_3 (1 - \nu_{12}\nu_{21}) / \Delta$$

$$C_{21} = E_2 (\nu_{12} + \nu_{13}\nu_{32}) / \Delta, \; C_{31} = E_3 (\nu_{13} + \nu_{12}\nu_{23}) / \Delta, \; C_{32} = E_3 (\nu_{23} + \nu_{13}\nu_{21}) / \Delta$$

$$C_{12} = E_1 (\nu_{21} + \nu_{31}\nu_{23}) / \Delta, \; C_{13} = E_1 (\nu_{31} + \nu_{21}\nu_{32}) / \Delta, \; C_{23} = E_2 (\nu_{32} + \nu_{31}\nu_{12}) / \Delta$$

$$C_{44} = G_{23}, \quad C_{55} = G_{13}, \quad C_{44} = G_{12},$$

with $\Delta = 1 - \nu_{12}\nu_{21} - \nu_{23}\nu_{32} - \nu_{31}\nu_{13} - 2\nu_{12}\nu_{23}\nu_{31}$.

3.1.1 Dilatational Waves

First, consider the case where u_1 is the only non-zero displacement and an arbitrary pulse is moving in the x_1-direction with a velocity c_1. Then, u_1 can be written as

$$u_1 = f(x_1 - c_1 t) \tag{21}$$

where f is an arbitrary function. Then, $\varepsilon_{11} \neq 0,\ \varepsilon_{22} = \varepsilon_{33} = \varepsilon_{23} = \varepsilon_{31} = \varepsilon_{12} = 0$, and the first equation of motion (Eq. 18) becomes

$$C_{11}\, u_{1,11} = \rho \ddot{u}_1 \tag{22}$$

which is the one-dimensional wave equation. Substituting Eq. (21) into Eq. (22) gives the wave velocity

$$c_1 = \sqrt{C_{11}/\rho}. \tag{23}$$

Using the same approach, if u_2 is the only non-zero displacement and the wave front is moving in the x_2-direction with a velocity c_2. With $u_2 = f(x_2 - c_2 t)$, ε_{22} is the only non-zero strain component and the second equation of motion becomes

$$C_{22}\, u_{2,22} = \rho \ddot{u}_2 \tag{24}$$

and the velocity of dilatational waves in the x_2-direction is

$$c_2 = \sqrt{C_{22}/\rho} \tag{25}$$

Similarly, if u_3 is the only non-zero displacement and the wave front is moving in the x_3-direction with a velocity c_3. With $u_3 = f(x_3 - c_3 t)$, ε_{33} is the only non-zero strain component and the third equation of motion becomes

$$C_{33}\, u_{3,33} = \rho \ddot{u}_3 \tag{26}$$

and

$$c_3 = \sqrt{C_{33}/\rho} \tag{27}$$

This shows that for orthotropic materials, for dilatational waves propagating in the material principal directions, the equations of motion uncouple and three different wave velocities are obtained (Eqs. 23, 25 and 27). For isotropic materials, the wave velocity is the same in all directions and is given by

$$c = \sqrt{\frac{E(1-\nu)}{\rho(1+\nu)(1-2\nu)}} \tag{28}$$

With this type of body waves where a planar wave front propagates in an unbounded solid, behind the wave front the body is in a state of plane strain. For a thin rod under axial stress, the material is in a state of plane stress and the stress strain relation is Hooke's law ($\sigma = E\varepsilon$). In that case, waves propagate in the axial direction with the velocity

$$c_o = \sqrt{E/\rho} \tag{29}$$

which is sometimes called the rod velocity. For steel, Poisson's ratio is 0.3 so, using the last two equations we find that $c/c_o = 1.160$ which is a significant difference.

3.1.2 Shear Waves

When u_1 is the only non-zero displacement and the wave front is moving in the x_2-direction with a velocity c_4. Then, u_1 can be written as

$$u_1 = f(x_2 - c_4 t) \tag{30}$$

where f is an arbitrary function. Then, $\varepsilon_{12} \neq 0,\ \varepsilon_{11} = \varepsilon_{22} = \varepsilon_{33} = \varepsilon_{23} = \varepsilon_{31} = 0$, and the first equation of motion becomes

$$G_{12}\, u_{1,22} = \rho \ddot{u}_1 \tag{31}$$

which is the one-dimensional wave equation. Writing Eq. (30) as $u_1 = f(\eta)$ where $\eta = x_2 - c_4 t$, we find that $u_{1,22} = f''$ and $\ddot{u}_1 = c_4^2 f''$ where a prime indicates a derivative with respect to η. Substituting into Eq. (31) gives the shear wave velocity $c_4 = \sqrt{G_{12}/\rho}$. Similarly, when u_1 is the only non-zero displacement and the wave front is moving in the x_3-direction with a velocity c_5. Then, u_1 can be written as $u_1 = f(x_3 - c_5 t)$. ε_{31} is the only non-zero strain and substituting into the first equation of motion gives $c_5 = \sqrt{G_{13}/\rho}$. When $u_2 = f(x_3 - c_6 t)$, substituting into the second equation of motion gives $c_6 = \sqrt{G_{23}/\rho}$.

Substituting $u_2 = f(x_1 - c_4 t)$, $u_3 = f(x_1 - c_5 t)$, or $u_3 = f(x_2 - c_6 t)$ into the equations of motion will also give the three shear wave velocities

$$c_4 = \sqrt{G_{12}/\rho},\ \ c_5 = \sqrt{G_{13}/\rho},\ \ c_6 = \sqrt{G_{23}/\rho} \tag{32}$$

For an isotropic material the three shear moduli are the same so the three shear wave velocities are the same.

3.2 Surface Waves

The body waves discussed in the previous subsection reflect after reaching a boundary of the solid. There are also several types of waves that propagate along the surface of the body. Here we recall some basic results for three types of surface waves: Rayleigh waves, Scholte-Stoneley waves, and Franz waves. Rayleigh waves are disturbances that propagate along the surface of a solid with amplitudes that decay exponentially with depth. In this section we recall existing results for the c_R, phase velocity of Rayleigh waves, and approximate expressions that show that those waves propagate at speeds that are slightly lower than the phase velocity of bulk shear waves in the solid. At the interface between a liquid and a solid, Rayleigh waves can be excited by an incident wave in the fluid. These waves propagate along the interface with a velocity c_R and radiate back into the fluid. They are called leaky Rayleigh waves.

Stoneley waves are waves that propagate along the interface between two solids with amplitudes that decay exponentially away from the interface. When the interface separates a solid from a fluid these waves are called Scholte-Stoneley waves or simply Scholte waves. Such waves are observed during the interaction of an underwater blast and a structure.

For curved bodies such as spheres and cylinders, the surface of the body is divided into an illuminated region that can be reached by the incident wave and a shadow region. Franz waves (or creeping waves) start from the edges of the illuminated region, propagate into the shadow zone following the curvature of the body and then radiate in a tangential direction. These waves propagate in the fluid at the speed of sound in the fluid.

3.2.1 Rayleigh Waves

In a solid, Rayleigh waves [42] are surface waves in which the motion is localized in a thin layer near the surface with a thickness approximately equal to twice the wavelength of the wave [33]. The horizontal and vertical components of the motion are 90° out of phase and the trajectories of the particles are ellipses with a major axis perpendicular to the surface. The amplitude of these waves decay exponentially with the distance from the free surface and $c_{R,}$ the speed of Rayleigh waves, is the solution of the equation

$$\left(2-\frac{c_R^2}{c_T^2}\right)^2 = 4\sqrt{1-\frac{c_R^2}{c_T^2}}\sqrt{1-\gamma\frac{c_R^2}{c_T^2}} \tag{33}$$

where $\gamma = \mu/(\lambda + 2\mu)$. The phase velocity of Rayleigh waves c_R is slightly lower than the phase velocity of transverse waves (shear waves) c_T and it depends of Poisson's ratio. A good approximation for the phase velocity of Rayleigh waves is given by

$$c_R = c_T\ (0.862 + 1.14\nu)/(1+\nu) \tag{34}$$

used by Jagnoux and Vincent [43], or the following approximations

$$c_R = c_T\ (0.87 + 1.12\,\nu)/(1+\nu) \quad c_R = \left(\frac{0.44+K}{0.58+K}\right)^{1/2} c_T \tag{35-a,b}$$

given by Viktorov [38] and Royer and Clorennec [44] respectively where $K = \nu/(1+\nu)$. Many other such approximations can be found in the literature [e.g. 45–58].

When the solid surface is in contact with a fluid, the Rayleigh wave propagating along the surface of the interface induces waves in the fluid. In this case, the wave is called a leaky Rayleigh wave or a generalized Rayleigh wave. The motion of particles near the interface is elliptical in both the fluid and the solid. Leaky Rayleigh waves are used for ultrasonic imaging of surface defects in materials [43]. They also are observed during the diffraction of a shock wave by an elastic solid.

Considering a solid immersed in water, a wave propagating in the water at a speed $c_1 = 1{,}498$ m/s at an incident angle i_1 will generate two waves in the solid with phase velocities c_2 and c_3 and their respective angles i_2 and i_3. In addition, for the proper value of i_1, Rayleigh waves will propagate along the surface ($i_R = 90°$) with a velocity c_R. According to Snell's law,

$$\frac{\sin i_1}{\sin i_k} = \frac{c_1}{c_k} \tag{36}$$

where $k = 2{,}3$ for bulk waves and $k = R$ for Rayleigh waves. For steel $E = 210$ GPa, $\rho = 7{,}850$ kg/m^3 so $c_2 = 3{,}208$ m/s for shear waves and $c_3 = 5{,}172$ m/s for longitudinal waves. Using Eq. (34), for a Poisson's ratio of 0.3, the velocity of Rayleigh waves is $c_R = 0.9262\, c_2 = 2{,}971$ m/s compared to 2,990 m/s in [43]. Equation (36) indicates that $i_2 = 90°$ when $\sin i_1 = c_1/c_R$ or $i_1 = 30.3°$. The incident wave in the fluid excites Rayleigh waves for an incident angle of $\theta_R = 30°$.

The amplitude of leaky Rayleigh waves decays rapidly with the distance travelled along the solid-water interface because of energy radiation into the liquid. This is in contrast with the propagation of Rayleigh waves on the surface of a solid in air where no such attenuation takes place.

Neuenschwander et al. [59] showed that the phase velocity of leaky Rayleigh waves should be between that of the Rayleigh wave in air and that of the transverse wave in the solid $c_R \le c_{LR} \le c_T$. The experiments of Goodman, Bunney and Marshall [60] showed that when an acoustic beam reaches the surface of a cylinder at an angle θ_R, leaky Rayleigh surface waves are generated, as in the case of a plate, and the amplitude of the portion of that wave radiated in the fluid is maximum when the receptor is located at an angle θ_R from the radial direction. The measured velocity of θ_R the Rayleigh wave was 3,280 m/s for a solid aluminum cylinder in water and the measured θ_R angle 28°.

Formulas such as (33, 34, 35-a,b) for calculating the velocity of Rayleigh waves were derived assuming that the surface of the solid was flat. Several authors examined how the curvature of the surface of a cylinder affected the speed of Rayleigh waves. According to Szilard [61], on circular cylinders, Rayleigh waves propagate in the circumferential direction with a velocity

$$c = c_R\left(1 + \frac{\lambda}{2\pi R}\right) \tag{37}$$

where c_R is the velocity on a flat surface, λ is the wavelength and R is the radius of the cylinder. The analysis of Jin, Wang and Kishimoto [62] indicated that

$$c = c_R\left(1 + 0.4822\,\frac{\lambda}{2\pi R}\right) \quad c = c_R\left(1 - 1.1429\frac{\lambda}{2\pi R}\right) \tag{38-a,b}$$

in the circumferential and axial directions respectively. These three formulas show that the effect of curvature become negligible when the wavelength is short compare to the radius of curvature.

Experiments conducted by Bunney et al. [63] showed that as a solid cylinder is progressively made hollow, the circumferential acoustic waves that can be excited change from having characteristics of Rayleigh waves to having the characteristics of Lamb waves. It is also possible to excite both Rayleigh- and Lamb-type waves [64–68].

3.2.2 Scholte-Stoneley Waves

Disturbances propagate near a free surface (Rayleigh waves) but also near the interface between two half-spaces. Stoneley [69] pointed out the existence of a wave propagating along the interface between two elastic solids. In this case, the amplitudes decrease with x_2 away from the interface $x_2 = 0$. The geophysicist Scholte [70] described a particular case of the Stoneley wave when one of the solid becomes a fluid. This wave, called the Scholte-Stoneley wave, has its energy mainly localized in the fluid and, if the viscosity of the media is negligible, it propagates without attenuation [71]. The wave is of maximum intensity at the interface and decreases exponentially away from the interface into both the fluid and the solid medium. Near the interface, particles move on elliptical trajectories. In the solid, the major axis of the ellipses are perpendicular to the interface while in the water they are parallel to the interface.

Considering a fluid–solid interface where the fluid being located above the interface and the solid below the interface ($x_2 < 0$), the phase velocity of the Stoneley wave is determined from the algebraic equation [72]

$$\left(\frac{\rho_1}{\rho_2} b_{2L} + b_1\right) r^4 - 4 b_1 r^2 - 4\, b_1\, (b_{2L} b_{2T} - 1) = 0 \tag{39}$$

where

$r = c_s/c_{2T}$, $b_1 = \left(1 - \frac{c_s^2}{c_1^2}\right)^{1/2}$, $b_{2L} = \left(1 - \frac{c_s^2}{c_{2L}^2}\right)^{1/2}$ and $b_{2T} = \left(1 - \frac{c_s^2}{c_{2T}^2}\right)^{1/2}$ .c_s is the phase velocity of the Stoneley wave, c_1 is the speed of sound in the fluid, c_{2L} and c_{2T} are the phase velocities of longitudinal and transverse waves in the solid. Meegan et al. [73] indicate that for several common examples of water-solid examples, the velocity of Scholte waves are only slightly lower than the speed of sound in water except for the sandstone-water example. The maximum phase velocity of the Scholte-Stoneley wave is approximated by

$$c_s = (1 - \varepsilon)\, c_f \tag{40}$$

where c_f is the speed of sound in the fluid and ε is a given by

$$\varepsilon = \frac{1}{8}\left(\frac{\rho_f}{\rho} \frac{c_f^2\, c_L^2}{c_T^2\, \left(c_L^2 - c_T^2\right)}\right)^2 \tag{41}$$

in terms of ρ_f, the density of the fluid, ρ, the density of the solid, and the longitudinal and transverse wave velocities in the solid c_L and c_T [71]. Therefore, Scholte-Stoneley wave the maximum speed of is usually slightly lower than the speed of sound in the fluid.

Experiments [74] showed that, at a water-glass interface, the Rayleigh wave is strongly attenuated while the Scholte wave (theoretically undamped) is weakly attenuated. The phase velocities were 3,091 m/s for the leaky Rayleigh wave and 1,488 m/s for the Scholte wave. The phase velocities for bulk waves in the glass were $c_L = 5{,}712$ m/s and $c_T = 3{,}356$ m/s. Surface waves at a plexiglass-water interface were also studied. In that example, the density of plexiglass is 1,190 kg/m^3, $c_L = 2{,}692$ m/s, $c_T = 1{,}407$ m/s and the predicted velocity of the Scholte wave is $c_S = 1{,}067$ m/s while the speed of sound in water is 1,500 m/s. This configuration is called a soft solid–fluid configuration because $c_T < c_W$. In this case, a bulk wave with a wave speed of 1,407 m/s was observed during experiments but no Rayleigh wave was detected. This is attributed to the fact that the acoustic velocity of water is larger than the transverse velocity of Plexiglass. When the same plexiglass is immersed in pure ethanol with a density of 790 kg/m^3 and an acoustic velocity of 1,115 m/s, a leaky Rayleigh wave with a phase velocity of 1,377 m/s was observed along with a Scholte wave with a velocity of 1,011 m/s. Weng and Yew [75] showed that underwater explosions generate Scholte-Stoneley surface waves at the interface between the water and an ice cover.

A review of the acoustics of shells [76] discusses the dispersion curves for Lamb waves on free plates and for fluid-loaded plates. For plates with one-sided water loading, a Scholte-Stoneley wave called the A wave appears. It is due to the fluid loading and is largely water-borne. When the plate is loaded with one fluid on one side and a different fluid on the other side, there are two Scholte-Stoneley waves [77].

Experimental results from short-pulse of scattering of water-immersed thin-walled cylindrical shells filled with air, water or alcohol [78] provide evidence of the existence of two Scholte-Stoneley waves for double fluid loading. Since the speed of sound is 1,480 m/s in water and 1,200 m/s in alcohol, the two Scholte-Stoneley waves could be clearly distinguished in the back scattering signals. Bao, Raju, and Uberall [79] also studied a submerged cylindrical shell with a different fluid inside.

Uberall et al. [66] presented an overview of the dispersion curves for Lamb waves and Scholte-Stoneley waves on thin, water-loaded and evacuated shells made of aluminum, stainless steel and tungsten carbide. Kim and Ih [80] determined the dispersion curves for the Scholte-Stoneley and Lamb waves of boron-aluminum composite shells immersed in water analytically and experimentally. Maze and co-workers [81, 82] studied the propagation of Scholte-Stoneley waves on submerged cylindrical shells.

3.2.3 Franz Waves

Franz [83] first showed that the scattering of waves by a cylinder immersed in water consist of a specular reflection and two waves with velocities lower that the free-wave velocity in water that circumnavigate the cylinder one in the clockwise and one in the counterclockwise direction (Bunney, Goodman and Marshall [63]). The first experimental evidence of those waves that Franz called creeping waves was provided by Barnard and McKinney [84]. In the experiments conducted by Neubaeur [85, 86], the speed of creeping waves around a cylinder submerged in water was 99% of the speed of sound in water.

Ahyi et al. [87] first presented shadowgraphs of the interaction of an incident wave with a cylinder submerged in water. Figures clearly show the incident wave, the specularly reflected wave, the creeping wave and both symmetric and anti-symmetric Lamb waves. Further experimental visualization results for creeping waves were provided by Latard et al. [88] for scattering by a glass sphere. Neubauer [89] presented experimental results and graphical methods for determining the shape of the reflected wave front, the creeping wave front and the wavefront produced by leaky Rayleigh waves during the diffraction of acoustic waves by an elastic cylinder. When the incident ray becomes tangent to the cylinder, a creeping wave is generated that travel in part around the circumference of the cylinder and then radiate into the water in the tangential direction. Keeping a constant travel time, the tip of the vector representing the final radiation into the water generates the wave front for the creeping wave.

Theoretical analyses of creeping wave were conducted by Überall, Doolittle, and McNicholas [90], Ugincius [91] and Ugincius and Uberall [92].

3.3 Lamb Waves

In an infinite elastic layer in which the top and bottom surface are stress free, two families of waves results from the combination of dilatational and shear waves reflecting from the free surfaces and Rayleigh waves propagating along these surfaces. These waves are usually called Rayleigh-Lamb waves or Lamb waves and for long wavelengths the lowest modes correspond to extensional or bending waves predicted by plate theories.

Wave propagation in isotropic solids can be studied in a more general way starting with the equations of motion (Eq. 18), the stress–strain relations

$$\sigma_{ij} = \lambda\, \varepsilon_{kk}\, \delta_{ij} + 2\mu\varepsilon_{ij} \tag{42}$$

where λ and μ are the two Lame constants of the material, and the strain–displacement relations

$$\varepsilon_{ij} = \left(u_{i,j} + u_{j,i}\right)/2 \tag{43}$$

Using Helmholtz's representation, the displacements can be written in terms of a scalar potential ϕ and a vector potential $\bar{\psi}$ so that

$$\bar{u} = \overline{\nabla\phi} + \bar{\nabla}\,x\,\bar{\psi} \tag{44}$$

so that the three components of the displacement vector are

$$u_1 = \frac{\partial \phi}{\partial x_1} + \frac{\partial \psi_3}{\partial x_2} - \frac{\partial \psi_2}{\partial x_3}$$

$$u_2 = \frac{\partial \phi}{\partial x_2} + \frac{\partial \psi_1}{\partial x_3} - \frac{\partial \psi_3}{\partial x_1}$$

$$u_3 = \frac{\partial \phi}{\partial x_3} + \frac{\partial \psi_2}{\partial x_1} - \frac{\partial \psi_1}{\partial x_2} \tag{45}$$

Substituting into the equations of motion gives

$$(\lambda + 2\mu)\ \nabla^2\phi - \rho\ddot{\phi} = 0 \tag{46}$$

$$\mu\nabla^2\bar{\psi} - \rho\ddot{\bar{\psi}} = 0 \tag{47}$$

These two equations are satisfied when the phase velocities for the longitudinal and transverse waves are

$$c_L = \sqrt{(\lambda + \mu)/\rho} \quad \text{and} \quad c_T = \sqrt{\mu/\rho} \tag{48}$$

These are the same velocities obtained in Sect. 3.1.

Lamb [64] studied the propagation of harmonic waves in isotropic layers. When the motion is restricted to the x_1-x_2 plane, Eq. (47) become

$$\frac{\partial^2\phi}{\partial x_1^2} + \frac{\partial^2\phi}{\partial x_2^2} = \frac{1}{c_L^2}\frac{\partial^2\phi}{\partial t^2}\ \frac{\partial^2\psi}{\partial x_1^2} + \frac{\partial^2\psi}{\partial x_2^2} = \frac{1}{c_T^2}\frac{\partial^2\psi}{\partial t^2} \tag{49}$$

For harmonic waves of the form

$$\phi = \Phi(x_2)\ \exp[i(kx_1 - \omega t)]\ \psi = \Psi(x_2)\ \exp[i(kx_1 - \omega t)] \tag{50}$$

there are two types of modes: (1) symmetric modes for which $\Phi = A_2 \cos(px_2)$ and $\Psi = B_1 \sin(qx_2)$; (2) anti-symmetric modes for which $\Phi = A_1 \sin(px_2)$ and $\Psi = B_2 \cos(qx_2)$ where $p^2 = \frac{\omega^2}{c_L^2} - k^2$ and $q^2 = \frac{\omega^2}{c_T^2} - k^2$. Relationships between the frequency ω and the wave number k are obtained by considering the boundary conditions on the top and bottom surfaces ($x_2 = \pm h$): $\sigma_{22} = \sigma_{12} \equiv 0$ which give

$$\frac{\tan(qh)}{\tan(ph)} = -\frac{4k^2pq}{\left(q^2 - k^2\right)^2} \text{ and } \frac{\tan(qh)}{\tan(ph)} = -\frac{\left(q^2 - k^2\right)^2}{4k^2pq} \tag{51}$$

for the symmetric and anti-symmetric modes respectively. These equations are known as the Rayleigh-Lamb equations. In the literature, the symmetric modes are designated as S_o, S_1, S_2, ... in order of increasing frequency. The anti-symmetric modes are designated as A_o, A_1, A_2, ... For long wavelengths ($k \rightarrow 0$) the first symmetric mode (S_o) called the "extensional mode" travels at the "plate velocity". In this regime the plate stretches in the direction of propagation and contracts correspondingly in the thickness direction. At higher frequencies, the phase velocity converge towards the Rayleigh wave velocity. The first axisymmetric mode (A_o) called the "flexural mode".

Osborne and Hart [65] obtained the dispersion curves of a steel plate in contact with water, an extension of Lamb's work for plates in air. The dispersion relations for cylindrical shells in air and in water were determined analytically and experimentally by Uberall et al. [66, 67]. Experimentally determined dispersion curves for A_o modes are given by Cheeke et al. [68].

4 Interactions Between Shock Waves and Submerged Structures

This section discusses two important points in our geometrical acoustics approach to the study of shock wave interactions with submerged structures. First we examine how underwater shock waves generate other types of waves as they interact with the shell and the fluid inside. A basic approach is presented for generating the position of the various wave fronts. Then we examine the evolution of the pressure on both faces of a plate loaded by an underwater shock wave. This example brings out significant differences in the response between two important practical cases in which the back face is contact with air or in contact with water. It is shown that for water-backed plates, the incident pulse appears to propagate through as if the plate was not there. This apparent transparency property is used in Sect. 5 to analyze shock wave interactions with cylindrical shells.

4.1 Initial Response of a Plate to a Shock Wave

This subsection discusses how underwater blasts excite surface waves and Lamb waves in submerged plates and shells. Previous studies providing direct experimental evidence of this phenomenon are reviewed and an example is given to illustrate how a simple geometrical approach can be used to predict the position of the various wave fronts as a function of time. Only a few studies are dealing with close-in explosions. An overview of the current state of knowledge is presented here.

4.1.1 Shock Wave Generates a Rayleigh Wave on the Surface of a Thick Plate

The propagation of leaky Rayleigh waves and Scholte waves at the interface of a liquid and an elastic solid has been studied extensively because of potential applications. Scholte waves are used to determine the properties of marine sediments down to hundreds of meters below the seafloor [93, 94], to detect objects buried in the seabed [95], to measure the thickness thin gold layer deposited on a silicon wafer [96], to size inaccessible parts of industrial structures [97] for example. Leaky Rayleigh waves are used extensively in non-destructive testing [98].

Interface waves can be excited by explosions or transient forces applied on the interface [99–101] or by implosions [102]. In the following example, surface waves at the interface between a thick glass plate and water are excited by a cylindrical wave generated by a transducer. In the experiments of Fu et al. [103], a cylindrical wave is emitted from a source S located in water domain in the upper half of the plane and glass occupies the lower half-space. The speed of sound in the water is taken to be 1,480 m/s. For glass, the density is 2,530 kg/m^3, the phase velocity of longitudinal waves is 5,690 m/s, the phase velocity of transverse waves is 3,460 m/s and the Rayleigh wave velocity is 3,180 m/s. The source is located 10 mm above the glass-water interface and the position of the various wave fronts after 12.5 μs is shown in Fig. 6. The incident wave is a circle of radius 18.5 mm centered at S. The reflected wave R is a circle centered at a point S′ symmetrically located below that interface. Figure 6 shows that, as the incident wave reaches the solid surface, a new wave front H called the head wave is created. In this example, the plate is quite thick so bending deformations are not induced. However, Rayleigh surface waves propagate along the interface and radiate back into the water. In a solid, Rayleigh waves are surface waves in which the motion is localized in a thin layer near the surface with a thickness approximately equal to twice the wavelength of the wave. The amplitude of Rayleigh waves decays exponentially with the distance from the free surface. A good approximation for the phase velocity of Rayleigh waves is

$$c_R = c_T \ (0.862 + 1.14\nu) \ /(1 + \nu) \tag{52}$$

where, for an isotropic solid, $c_T = \sqrt{G/\rho}$ is the phase velocity of shear waves in terms of the shear modulus G and the density ρ. When $\nu = 0.3$, $c_R = 0.926\, c_T$.

For the example in Fig. 6, a Rayleigh wave will be excited when the incident angle θ_i is such that the transmitted angle $\theta_t = 90°$ so that the reflected wave propagates along the interface. Using Snell's law,

$$\sin\theta_i \,/\, \sin\theta_t = c_f \,/\, c_R \tag{53}$$

we find that this angle is 27.74°. The solid-borne Rayleigh wave propagates along the interface at a speed c_R and then radiates back into the water at a 27.74° angle from the vertical to form what is called a head wave with a straight wave front at a 27.74° angle from the interface (Fig. 6).

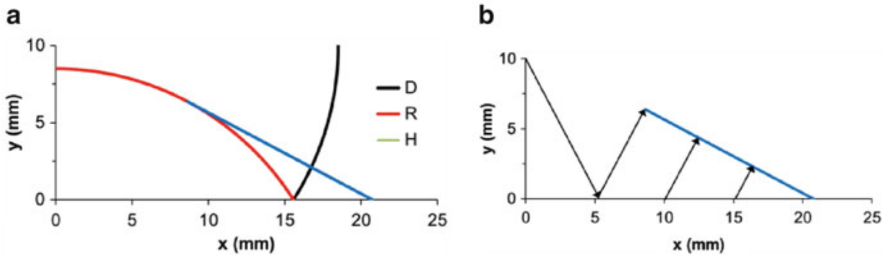

Fig. 6 Interaction of a shock wave generated by a transducer located at (0, 10) with a thick glass plate ($y < 0$). (**a**) Direct wave D, reflected wave R and a head wave H; (**b**) Rayleigh waves generated by an incided wave making a 27.74° with the vertical, travels along the interface ($y = 0$) and radiates back into the water ($y > 0$) at an angle of 27.74°

In this type of problem it the elastic solid is called soft if its shear wave velocity is smaller than the speed of sound in the liquid. Such a "soft solid–fluid" interface is found in the case of Plexiglas–water and PVC–water interfaces [74] and soft sea floors [101]. On the other hand, a "hard solid–fluid" configuration refers to a case in which speed of sound in the fluid is smaller than the shear velocity of the solid material as in the case of a glass-water interface. Theoretical and experimental investigations [74, 99–101] established that leaky Rayleigh waves do not propagate along a soft solid- fluid interface and in that case only a Scholte-Stonely surface wave propagates along the interface. Data from the propagation of Scholte waves is used to characterize the properties of sediments.

Alkier [104] showed that, at a critical incidence angle, an acoustic pulse can excite internally guided longitudinal stress waves in a submerged plate. In the case of an aluminum plate with a longitudinal wave velocity $c_L = 5.45 \times 103$ m/s immersed in water with water with $c_w = 1{,}484$ m/s, the critical angle obtained from Snell's law is $\theta_c = \sin^{-1}(c_w/c_L)$ or $\theta_c = 15.79°$ in this case.

4.1.2 Shock Waves Excite Lamb Waves in a Thin Plate

Leaky Lamb waves are used extensively in non-destructive evaluation [98]. There are other uses of this type of waves. For example, Bingham et al. [105] describe an approach using the propagation of Lamb waves to detect the presence of limpet mines on ship hulls. Ahyi et al. [87] presented experimental results for 1 mm thick steel plates in water subjected to a shock wave. In that case, both symmetric and anti-symmetric Lamb waves are excited and radiate back into the water. Ahyi et al. also considered 1 mm thick steel plates with water on both sides. Then, on the opposite side of the plate there is a wave front for the transmitted wave that is the mirror image of the reflected front R in Fig. 6 and the wave fronts corresponding to Lamb waves propagating along the plate.

4.1.3 Close-in Explosion

Wardlaw and Luton [106] described the fluid–structure interactions occurring when a charge explodes near a plate. Numerical analyses of close-in explosions near rigid surfaces, homogeneous plates, and sandwich plates are discussed in [107–110]. Similar studies for explosions inside water filled cylinders are presented in [106, 109, 111]. In all of these studies the explosion is modeled as a small initial cavity subjected to a given pressure. The initial shock wave propagates towards the structure, reflects, and interacts with the cavity. During the short duration of these simulations, the cavity representing the explosion bubble deforms very little due to the low frequency of the bubble oscillations

4.2 Long Term Response of a Plate to an Underwater Explosion

Here four related examples are considered in order to gain some insight into the dynamic response of plates subjected to impulsive loading. First we consider a plate subjected to a pressure pulse applied directly on the surface. When the time is much larger than the travel time through the thickness of the plate, the plate can be assumed to be rigid. In the second example, a semi-infinite solid is in contact with water and the loading consists of a pressure pulse propagating through the water. The pressure at the interface is the sum of the incident and reflected pulses and depends on the mechanical impedances of the water and the solid. In the third example, the semi-infinite solid is replaced by a plate of finite thickness in contact with air on the other side. In the fourth example, the plate is in contact with water on both sides.

4.2.1 Free Plate Subjected to a Pressure Pulse

Considering an infinite plate of thickness subjected to a step pressure on the left and free on the right, the Lagrange diagram of Fig. 7a shows the reflections of elastic waves from the two surfaces. In that figure the non-dimensional time $\bar{t} = t\,c/h$ is plotted versus the non-dimensional position $\bar{x} = x/h$ where h is the thickness of the plate, and c is the speed of sound in the material. Using the method of characteristics, we find that the particle velocity on the right face increases in a stair-case manner (Fig. 7b). The non-dimensional velocity is defined as $\bar{v} = v.\,\rho c/p_o$ where ρ is the density of the material and p_o is the suddenly applied pressure. If the plate is considered as a rigid body, the velocity of the plate is directly proportional to time ($\bar{v} = \bar{t}$) and the figure shows that the rigid body approximation is adequate for times much larger that h/c, the travel time through the thickness.

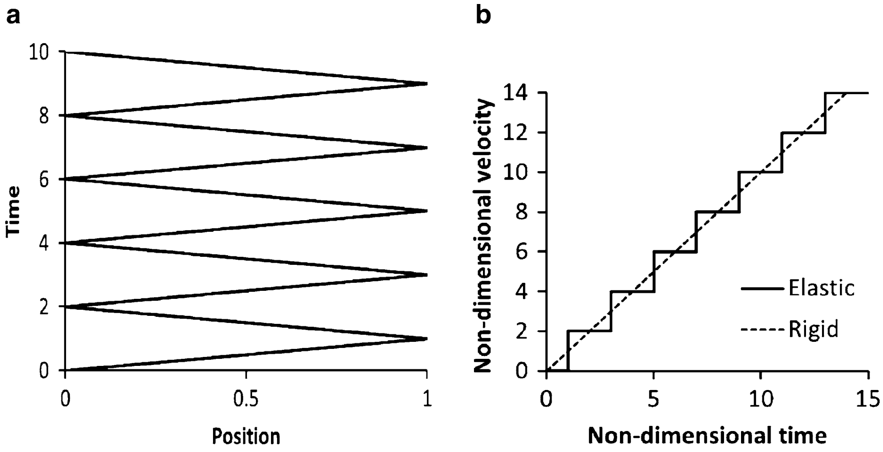

Fig. 7 Short term response of a plate subjected to step pressure pulse (**a**: Lagrange diagram; **b**: non-dimensional plate velocity versus time)

Considering the plate as a rigid body with a density ρ, a thickness h, and a surface area A that is completely free and subjected to a pressure pulse p(t) applied directly to its front face. V is the velocity at the end of the pulse, $\rho hA\,V$ is the linear momentum at the end of the pulse, and $I = \int p\,dt$ is the pressure impulse (per unit area). The impulse-momentum relation states that the momentum at the end of the impulse is equal to the applied impulse. Therefore, the velocity is

$$V = I/\rho h \tag{54}$$

When the plate is subjected to a step pressure, the impulse increases linearly with time. Equation (54) predicts that the velocity V also increases linearly with time as indicated by the dashed line in Fig. 7b. The rigid body approximation is adequate for times much larger that h/c, the travel time through the thickness. The kinetic energy of the plate is

$$T = \frac{1}{2}\rho h V^2 = \frac{1}{2}\rho h\left(\frac{I}{\rho h}\right)^2 = \frac{1}{2}\frac{I^2}{\rho h} \tag{55}$$

This equation indicates that the kinetic energy absorbed by the plate increases with the square of the impulse and is inversely proportional to the mass per unit area. For a given impulse, a heavy plate absorbs less kinetic energy than a light plate.

Fleck and Deshpande [112] describe the response of metallic sandwich structures to blast loading into three phases: in Phase I the applied impulse results in a uniform velocity of the first facesheet, Phase II corresponds to the crushing of the core material and phase III overall bending and stretching deformations of beam occurs.

Given the magnitude of the impulse I, Eq. (54) was used to determine the velocity of the front facesheet at the end of phase I [112]. Equation (55) is used without derivation by Pan and Watson [113]. It shows that the kinetic energy absorbed is proportional to the square of the impulse and inversely proportional to the mass per unit area. Therefore, for a given impulse, a heavier plate absorbs less kinetic energy than a lighter plate. We also note that the impulse is the quantity of interest regardless of the shape of the pressure versus time curve.

4.2.2 Wave Interaction at the Interface Between Water and a Solid

Underwater blasts generate shock waves that propagate through water before reaching the surface of a solid structure and reflecting off of that surface. The pressure at the water-solid interface is shown to be different from that of the incident pulse.

Figure 8a shows the one-dimensional problem of a pulse impinging on a water-solid interface with a normal incidence. The Lagrange diagram (Fig. 8b) shows the time-position domain is divided into three regions. Initially both the water domain ($x < 0$) and the solid ($x > 0$) are a rest (region O in the figure). Region I is the incident pulse and after the pulse reaches the interface the water and the solid have the same stress T (positive in compression) and particle velocity v (Region II). From the stress-velocity diagram (Fig. 8c) it can be easily shown that

$$T_2 = \frac{2z_s}{z_s + z_w} T_1 \tag{56}$$

where T_1 is the stress in region I, T_2 is the stress in region II, z denotes the mechanical impedance and the subscripts s and w refer to the impedance of the solid and the water respectively.

The speed of sound in water is approximately 1,500 m/s and the density 1,000 kg/m^3 so its mechanical impedance $z_w = 1.5 \times 10^6$ kg/m^2/s. For steel, with a modulus of elasticity of 210 GPa, a Poisson's ratio of 0.3 and a density of 7,850 kg/m^3, Eq. (28) predicts a speed of sound of 6,001 m/s. The mechanical impedance of steel $z_s = 47.11 \times 10^6$ kg/m^2/s is much larger than that of water and the ratio T_2/T_1 predicted by Eq. (56) is 1.938 which is very close to 2. Therefore, it is often said that upon reflection from a steel surface the pressure suddenly doubles as if that surface were rigid. Considering a typical composite material with a transverse modulus of 10.30 GPa and a density of 1,500 kg/m^3, the speed of sound is approximately 2,620 m/s, $z_s = 3.931 \times 10^6$ kg/m^2/s and from Eq. (56) we find that $T_2/T_1 = 1.448$. Therefore, the mechanical impedance of the composite material is closer to that of the water a much different behavior occurs: the pressure does not double as the wave reflects from the surface.

Considering a 5 mm thick steel plate in contact with air on the right hand side, the response to a step pressure wave is such that the pressure on the wet side decays

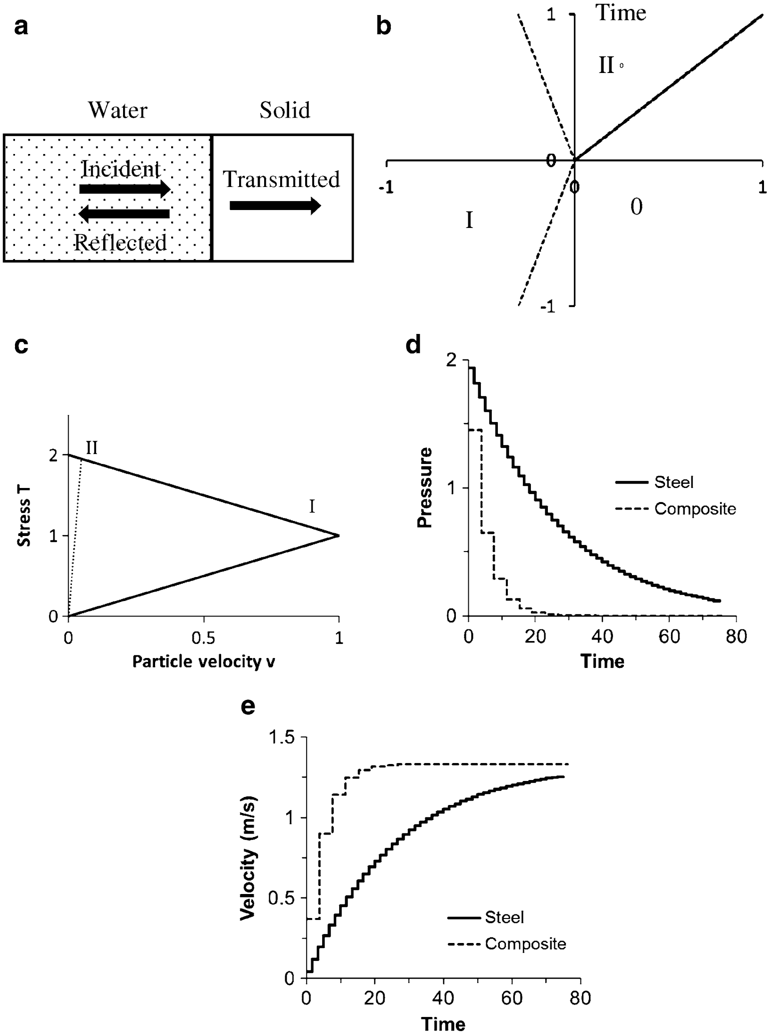

Fig. 8 Reflection and transmission of an incident wave at a fluid–solid interface. (**a**) Reflected and transmitted waves at a water-solid interface; (**b**) Lagrange diagram showing the incident wave in the fluid being reflected from the interface x = 0 and the transmitted wave in the solid (y > 0); (**c**) Stress velocity diagram where the slope of the *solid lines* is the impedance of water and the slope of the *dashed line* is the impedance of the solid; (**d**) Interface pressure (MPa) versus time (μs) for 5 mm thick air backed plates made out of steel or composite materials; (**e**) Interface velocity versus time (μs) for 5 mm thick air backed plates made out of steel or composite material

progressively to zero (Fig. 8d) and the velocity of that face increases progressively towards an asymptotic limit (Fig. 8e). The small steps in those curves are due to wave reflections inside the plate. For a 5 mm thick composite plate, the response is quite different as shown on these figures. Both the pressure and the velocity change

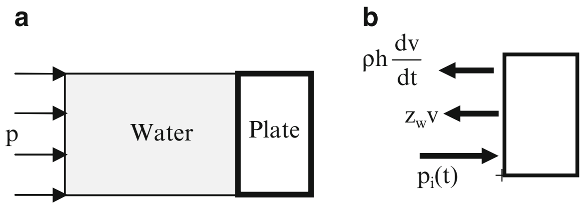

Fig. 9 One dimensional model of an air-backed plate (ABP) subjected to an incident pressure pulse (**a**: general configuration, **b**: Free body diagram of the plate)

more rapidly in a few large steps. These examples show that the response to an incident pulse transmitted through water is different than when the pressure pulse is applied directly to the plate. The response of a composite plate is significantly different because its mechanical impedance is much lower than that of steel.

4.2.3 Dynamic Response of an Air-Backed Plate to a Shock Wave

Now consider an exponentially decaying pulse $\left(p_i = p_o\, e^{-t/t_d}\right)$ propagating towards an air-backed plate (Fig. 9). Considering a unit area of the plate as a rigid body, two external forces are applied: one is caused by the incident and reflected waves $(p_i + p_r)$ and the other is due to the motion of the plate $(z_w v)$. The inertia force is equal to ρh, the mass per unit area, times the acceleration dv/dt. As discussed above, $p_r = p_i\,(2z_s)/(z_s + z_w)$ and, if the impedance of the solid is much larger than that of water, $p_r \approx p_i$.

Applying Newton's law, gives the equation of motion originally derived by Taylor [114] in 1941

$$\rho h \frac{dv}{dt} + z_w v = 2p_o\, e^{-t/t_d} \tag{57}$$

Solving Eq. (57) gives the velocity of the plate

$$v = \frac{2p_o}{z_w}\left(e^{-t/t_d} - e^{-t/t_o}\right) \Big/ \left(1 - \frac{t_o}{t_d}\right) \tag{58}$$

where the mechanical impedance $z_w = \rho_w c_w$ is the product of the density of the water and the speed of sound in the water. The constant $t_o = \rho h / z_w$ is called by Kirkwood the damping time of the plate (see Kennard [115]). The total pressure on the wet face of the plate is

$$\tilde{p} = 2p_o\, e^{-t/t_d} - z_w\, v = 2p_o\left(-\frac{t_o}{t_d} e^{-t/t_d} + e^{-t/t_o}\right) \Big/ \left(1 - \frac{t_o}{t_d}\right) \tag{59}$$

This pressure becomes zero for time t_m when $-\frac{t_0}{t_d} e^{-t_m/t_d} + e^{-t_m/t_0} = 0$ which gives

$$t_m = \frac{t_d}{\frac{t_d}{t_o} - 1} \ln \frac{t_d}{t_o} \tag{60}$$

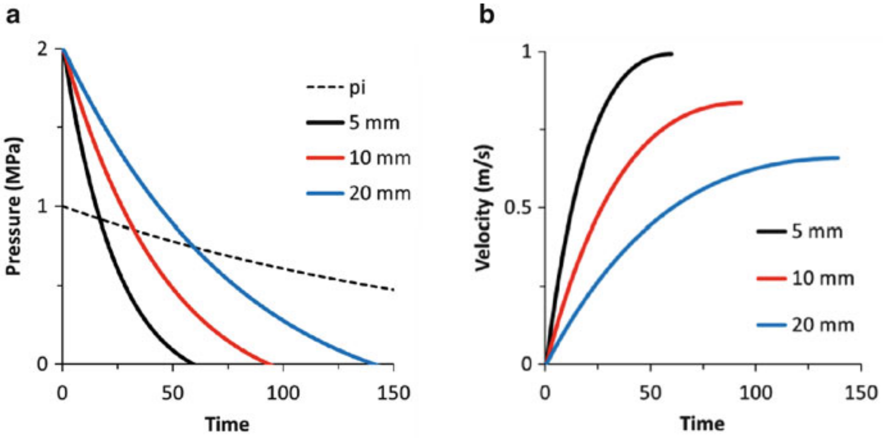

Fig. 10 Air-backed steel plate subjected to exponential pulse with $p_o = 1$ MPa, $t_o = 200$ μs. Pressure on the wet side of the plate and velocity as a function of time (μs) for three values of the thickness h

The velocity of the plate at that time is

$$v = \frac{2p_o}{z_w} e^{-t_m/t_d} = \frac{2p_o}{z_w} \left(\frac{t_d}{t_o} \right)^{1/\left(1 - \frac{t_d}{t_o}\right)} \tag{61}$$

Figure 10 shows results for a steel plate obtained assuming that the density of steel is 7,850 kg/m^3, the density of water is 1,000 kg/m^3, the speed of sound is 1,500 m/s, $p_o = 1$ MPa, and $t_o = 200\,\mu$s. On the wet surface of the plate, the pressure becomes negative once t exceeds the value t_m predicted by Eq. (60) which defines the limit of the model. Figure 10 shows that this cavitation occurs shortly after the plate velocity reaches its maximum.

The loss of contact with the fluid implies that the impulse I_o is not fully applied to the plate. The impulse transmitted to the plate is given by

$$I = \xi I_o \tag{62}$$

where $\xi = \psi^{\psi/(1-\psi)}$ and $\psi = t_d/t_o$. Kambouchev et al. [116, 117] extended Taylor's model to the case of explosions in air. In that case, the reflection coefficient for the shock wave reflecting from the front face of the plate varies between 2 and 8 instead of 2 for underwater explosions. In the work of Kennard [115] and Dawson and Sullivan [118], the plate rests on an elastic foundation.

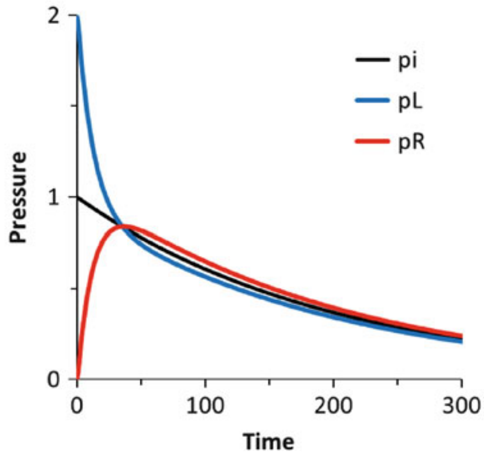

Fig. 11 Water-backed steel plate subjected to exponential pulse with $p_o = 1$ MPa, $t_o = 200$ μs. Incident pressure p_i and pressures on the *left* and *right* sides of the plate as a function of time (μs) for a thickness h = 5 mm

4.2.4 Water Backed Plates

The back face of the plate could also be in contact with water and in that case we will have a Water Backed Plate (WBP) as opposed to the Air backed Plate (ABP) previously considered. Both ABP and WBP were studied in [109, 111, 119, 120].

Equation 57 was developed for an air-backed plate, for a water backed plate, the mechanical impedance z_w should be replaced by $z'_w = 2\,z_w$ to account for the fact that there is water on both sides of the plate. The pressure on the back face is obtained by multiplying the plate velocity by the impedance z_w. With the same parameter used for the ABP, we consider a 5 mm thick WBP steel plate assuming that the density of steel is 7,850 kg/m^3, the density of water is 1,000 kg/m^3, the speed of sound is 1,500 m/s, $p_o = 1$ MPa, and $t_0 = 200$ μs. Figure 11 shows a very different behavior: after approximately 35 μs the pressures on both the left and the right surfaces of the plate are nearly identical to the incident pulse. For this reason, it is sometimes said that the plate is almost "transparent" to the wave. There is a reduction in the maximum amplitude and, while the incident wave is a shock wave since it rises instantly from zero to its maximum pressure, the pressure pulse on the left rises progressively. It can also be seen that the pressure on the left surface remains positive.

5 Shock Wave Interactions with Submerged Shells

5.1 Previous Studies

The effect of shock waves on submerged cylindrical or spherical shells has been studied for many years because of naval applications. Without attempting an exhaustive review, we note the analytical approaches of Huang and co-workers

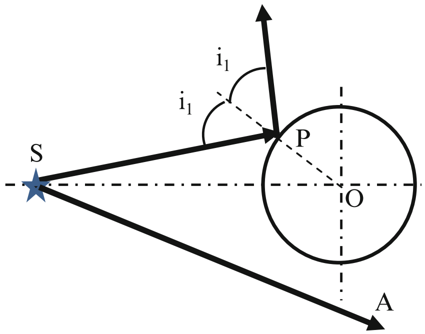

Fig. 12 Geometry of the problem. The explosion source S is located at a distance D = 5R to the *left* of a cylindrical shell of radius *R*. Lines *ST1* and *ST2* define the illuminated and shadow regions of the shell

[121–130], Payton [131], Tang and Yen [132], the analytical and numerical analyses in [133–139] and the experimental results of Hung et al. [140, 141]. In these references, pressure, velocity or acceleration at a few points around the shell is plotted as a function of time. Ref. [131] gives one figure showing the position of various wave fronts at one particular instant. Detailed studies of the interaction of shock waves with submerged cylindrical shells showing the progression of the various wave fronts as a function of time were presented by Iakovlev [142–153], Leblond et al. [154–158], Hasheminejad [159–161], and others [162–164].

5.2 *Interaction of a Cylindrical Wave with an Evacuated Shell*

Considering the interaction of a shock wave with a submerged air-filled cylindrical shell, this subsection presents an approach to determine the position of several wave fronts in the surrounding water. Wave fronts due to the direct, reflected and creeping waves propagating in the water and those due to waves radiated in the fluid because of the motion of the shell are determined using a ray tracing procedure.

With the geometry used in Iakovlev [142–153], a cylindrical shell of radius R is subjected to a cylindrical shock wave emanating from a source located at a distance $D = 5R$ from the axis of the shell (Fig. 12). From the source S, drawing two lines ST_1 and ST_2 tangent to the surface of the shell, defines the illuminated region T_1LT_2 and the shadow region T_1RT_2 of the shell. In the fluid, the region delimited by the two tangents and located to the right of the arc T_1RT_2 is called the shadow zone.

The shock wave propagates in all directions at the speed of sound in the water. The direct wave front, undisturbed by the presence of the shell, is a circle of radius r centered at S and SA is a typical ray (Fig. 13). The shock wave interferes with the shell when $r > D\text{-}R$. Then, rays reaching a point P in the illuminated region is reflected so that the reflected angle i_2 is equal to the incident angle i_1 and the total length $SP + PB = SA = r$. The wave fronts for the direct wave and the reflected wave labeled D and R in Fig. 14 are drawn using this ray tracing procedure. Following

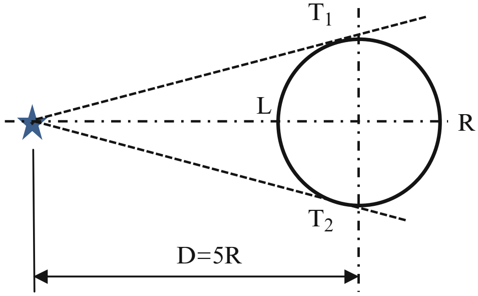

Fig. 13 Generation of a direct wave front by rays not interfering with the shell (ray *SA*) and reflected wave fronts (ray *SPB*)

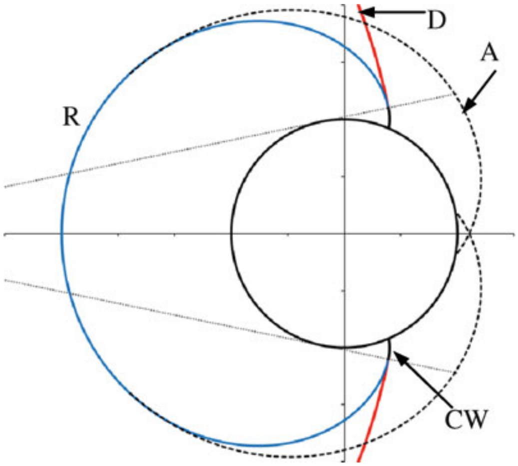

Fig. 14 Wave fronts generated by the interaction of a cylindrical shock wave and a cylindrical air-filled shell for d/R = 1.5 (*D* Direct wave, *R* reflected wave, *CW* creeping wave, *A* anti-symmetric radiated wave)

the same convention as in [142–153] we define the penetration distance $d = r\text{-}D + R$ and plot the position of the various wave front for $d/R = 1.5$ as in Ref. [147]. The D and R wave fronts meet along the tangents from the source to the shell. The curve joining that point to the surface of the shell is the wave front for the creeping waves in the shadow zone.

Creeping waves also known as Franz waves propagate in the shadow zone as the speed of sound in the fluid. As illustrated in Fig. 15, starting from the tangent point T1, a creeping wave propagates along the circumference and then radiates into the fluid in a tangential direction. The total length $ST_1 + T_1Q + QC$ is equal to r. When $T_1Q = 0$, the creeping wave meets the direct wave and reflected wave fronts and when $ST_1 + T_1Q = 0$, it reaches the surface of the shell.

The shock wave excites the propagation of waves in the shell along the circumferential direction. The lowest symmetrical and anti-symmetrical modes are excited. Anti-symmetrical modes tend to propagate at speeds near that of shear waves in a solid. In the calculations we assume a shear wave speed $c_2 = 3{,}100$ m/s in steel and a speed of sound of 1,480 m/s in water. Figure 16 shows an incident

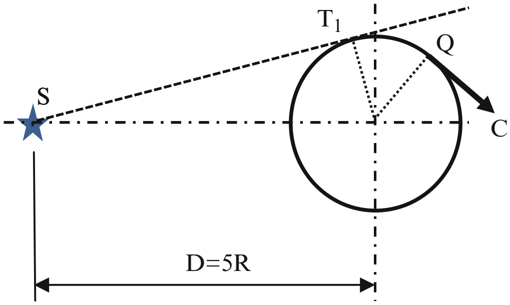

Fig. 15 Ray tracing procedure for creeping waves in the shadow region of cylindrical shell

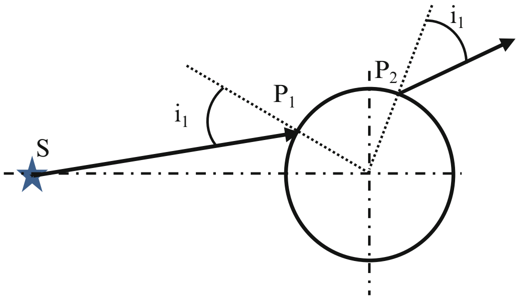

Fig. 16 Ray tracing procedures for waves caused by oscillations of the shell

ray SP1 making an angle i_1 with the radial direction. If this ray excites waves propagating in the circumferential direction, that is with a refracted angle i_2 of 90°, according to Snell's law, the critical angle for exciting the oscillations of the shell wall is given by

$$\sin i_1 = c_1 / c_2 \tag{63}$$

which gives a value of 28.52° in this case. Then, anti-symmetric waves in the shell propagate along the circumference with a velocity c_2 (arc P_1-P_2 in Fig. 16) and radiate back into the fluid at an angle i_1 as shown. The total length $SP_1 + P_1P_2 (c_2/c_1) + P_2D$ is equal to r, the radius of the direct wave front. The two radiated wave fronts shown in Fig. 14 are drawn using this ray tracing procedure. Symmetric modes for the shell tend to propagate at speeds near that of longitudinal waves in a solid: about 5,000 m/s for steel. The same procedure can be used to obtain those wave fronts.

The procedure presented here yield results that are in excellent agreement with those of Ref. [146] for this particular example and can be applied successfully to examples from [142–164]. The four types of wave fronts shown in Fig. 14 are predicted accurately without having to solve a complex fluid–structure interaction problem. Another advantage is that it brings insight into the physics of the problem. With a numerical approach, the interpretation of the results is not always clear.

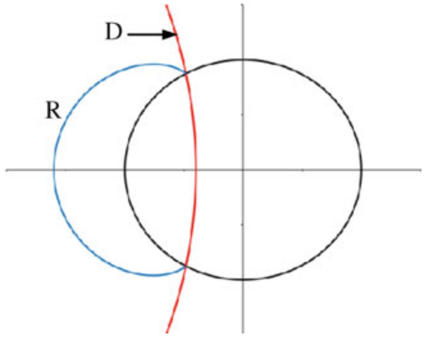

Fig. 17 Interaction with a fluid-filled cylindrical shell. Sonic case: d/R = 0.6, $c_2/c_1 = 1$. Direct and reflected wave fronts

5.3 *Interaction of a Cylindrical Wave with a Fluid-Filled Shell: Sonic Case*

Considering the interaction of a shock wave generated by an underwater explosion with a submerged cylindrical shell, we examine the case in which the liquid inside the shell is the same as the liquid surrounding it ($c_2/c_1 = 1$). Since the shell is filled with a liquid, waves will propagate through the inside fluid, they will in part reflect from the inside surface of the shell and inpart be transmitted back into the outside fluid. Therefore, there will be several new wave front in addition to those discussed in Sect. 5.2.

In Fig. 17, d/R = 0.6 and the shell is "transparent" to the direct wave in the sense that the wave front propagates through as if the shell was not there. The position of the wave front for the reflected wave is not affected by the presence of the inside fluid. Rays emanating from the source S do not reflect from the inside surface of the shell until the direct wave reaches the tangent point T1 (Fig. 12). This occurs when $r = \sqrt{D^2 - R^2}$ or $r = R\sqrt{24}$ for the present geometry. In other words, internal reflections will occur when

$$\frac{d}{R} > \sqrt{\frac{D^2}{R^2} - 1} - \left(\frac{D}{R} - 1\right) \tag{64}$$

In this case, D/R = 5 so we must have $d/R > \sqrt{24} - 4 = 0.89898$ for waves to reflect from the inside of the shell.

For a larger value of the d/R ratio (d/R = 1.7), we also note the presence of creeping waves in the outside fluid and of an additional wave front in the inside (Fig. 18). This new wave front is due to the reflection of rays from the inside surface of the shell. It is called R_1 because the rays reflect from the inside surface only once. This wave front has a cusp singularity and it starts where the direct wave crosses the shell (Fig. 18b). That figure also indicates that the R_1 wave front does not meet the CW wave front as they cross the shell.

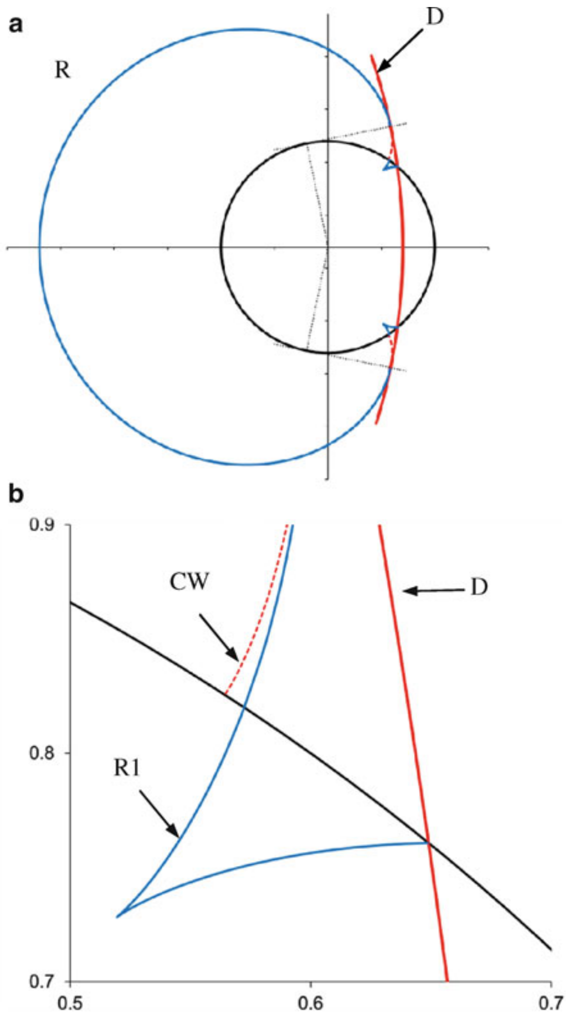

Fig. 18 Interaction with a fluid-filled cylindrical shell. Sonic case: d/R = 1.7, $c_2/c_1 = 1$. (**a**) general view; (**b**) expanded view

The R_1 wave front is drawn as indicated in Fig. 19. For a given value of the angle θ, the distances SA and AE are given by

$$SA = R\sqrt{\frac{D^2}{R^2} + 1 - 2\frac{D}{R}\ \cos\theta}\ AE = 2R\ \cos\ (\gamma)$$

where $\gamma = \sin^{-1}\left(\frac{D}{SA}\sin\theta\right)$ is the angle between both SA and AE and the radial direction. The distance from E to the center of the center of the shell given by

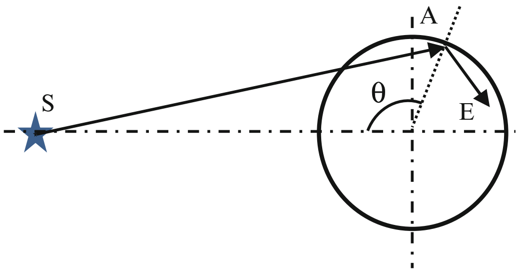

Fig. 19 Ray tracing procedure for the first reflected wave front R_1

$$OE = R\sqrt{1 + \left(\frac{D}{R} - 1 + \frac{d}{R}\right)^2 - 2\left(\frac{D}{R} - 1 + \frac{d}{R}\right)\cos(\gamma)}$$

when D/R = 5 and d/R = 1.7, OE $\leq$ 1 when $94.3^o \leq \theta \leq 130.5^o$. With this construction, when $78.46^o \leq \theta \leq 94.3^o$, point E is located outside the shell which means that this reflected ray has reached the inside surface of the shell and has been in part transmitted into the outside fluid and in part reflected back inside. The R1 wave front outside the shell is seen to meet the CW and D wave fronts along ST_1, the tangent to the circle. The wave front corresponding to the second reflection from the inside of the shell is too small to be drawn on this figure.

When d/R = 2.2, the size of the two R_1 wave fronts became larger and joined together and we note the presence of two additional wave fronts labeled R_2 (Fig. 20). R_2 indicates that those wave fronts are obtained by considering rays that reflect from the inside surface of the shell twice. R_2 wave fronts start where the R_1 wave fronts cross the shell. Figure 20b shows how the R_1 front meets the CW and D fronts in the outside fluid. The R_2 front follows the same pattern in the outside fluid but that part is not drawn here to keep the figure legible.

When d/R = 2.9, the R_1 wave fronts are no longer singular (Fig. 21). In that case, two R_3 wave fronts also appear and we see that the R_1 wave fronts are connected to two R_2 wave fronts which in turn are connected to the R_3 wave fronts. The R_3 wave fronts do not quite reach the CW front which indicates that there are R4 fronts which are not shown here because they are very small. Results shown in Figs. 19, 20 and 21 for cases where d/R = 1.7, 2.2, and 2.9 are in excellent agreement with those shown by Iakovlev et al. [143].

Figure 22 shows that inside the shell, the first reflected rays form a caustic in the upper right quadrant. That figure also shows that the singular points of the R_1 wave fronts are located on that caustic when d/R = 1.7 and 2.2. For d/R = 2.9, there is no singular point since the wave front goes beyond the caustic. Similarly, Fig. 23 shows the caustic generated after two reflections from the inside surface and the R_2 fronts for d/R = 2.2, 2.9, and 4.21. All three of these wave fronts have a singular point located on the caustic.

Results in Figs. 24 and 25 are in good agreement with those in Iakovlev et al. [143].

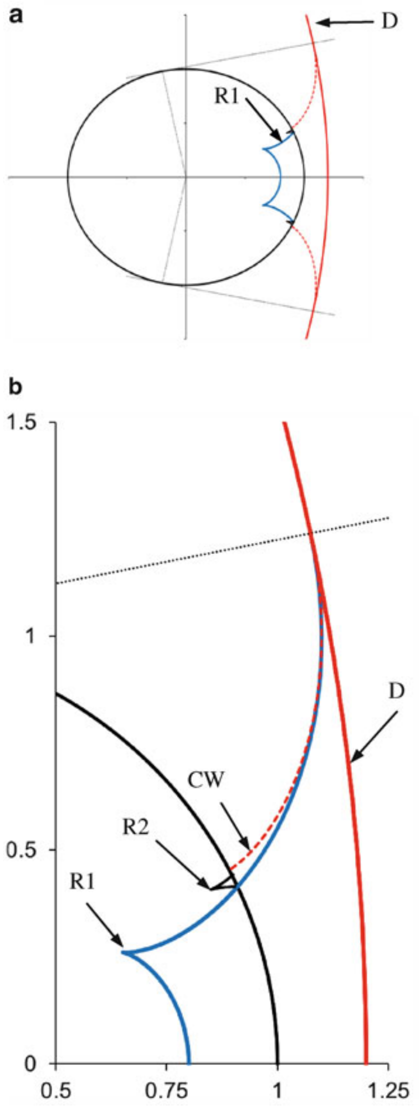

Fig. 20 Interaction with a fluid-filled cylindrical shell. Sonic case: d/R = 2.2, $c_2/c_1 = 1$. (**a**) general view; (**b**) expanded view

5.4 Interaction of a Cylindrical Wave with a Fluid-Filled Shell: Subsonic Case

When waves propagate slower in the inside fluid than in the outside ($c_2/c_1 < 1$) fluid different phenomena occur. In the present example, $c_2/c_1 = 0.43$. Figure 26 shows a different shape for the direct wave inside the shell compared to Fig. 17. This reflects

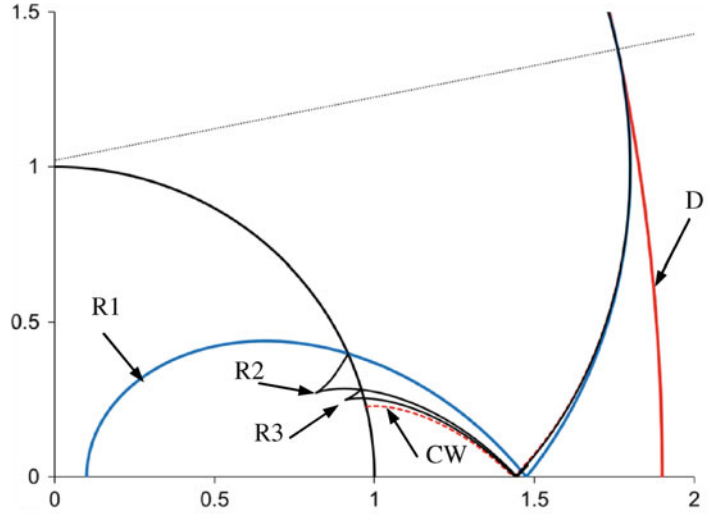

Fig. 21 Interaction with a fluid-filled cylindrical shell. Sonic case: $d/R = 2.9$, $c_2/c_1 = 1$

Fig. 22 Caustic and R_1 reflected wave fronts for $d/R = 1.7$ (*red*), 2.2 (*blue*), 2.9 (*black*). Sonic case, $c_2/c_1 = 1$

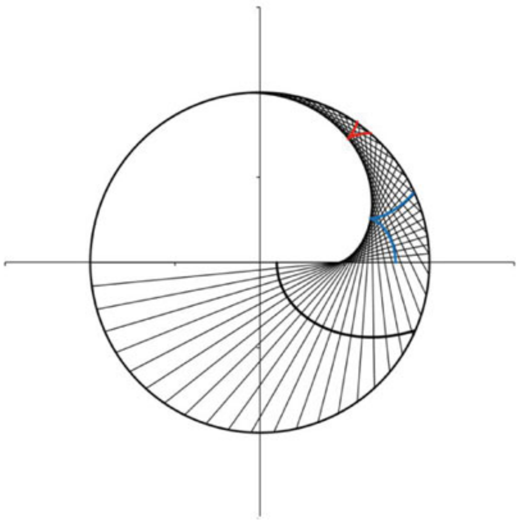

the fact that waves propagate at slower speeds inside. From Fig. 27 we find that, for a given angle θ, the angles α, i_1 and i_2 are given by

$$\alpha = \tan^{-1}\left[\sin\theta \,/\left(\tfrac{D}{R} - \cos\theta\right)\right],\ i_1 = \theta + \alpha,\ i_2 = \sin^{-1}\left(\frac{c_2}{c_1}\sin i_1\right) \tag{65}$$

The penetration distance is $AF = \frac{c_2}{c_1} R\left\{\frac{D}{R} - 1 + \frac{d}{R} - \sqrt{\frac{D^2}{R^2} + 1 - 2\frac{D}{R}\cos\theta}\right\}$.

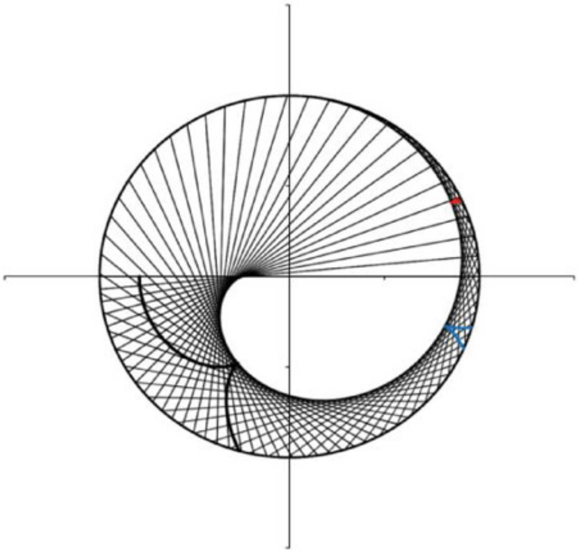

Fig. 23 Caustic and R_2 reflected wave fronts for $d/R = 2.2$ (*red*), 2.9 (*blue*), 4.21 (*black*). Sonic case, $c_2/c_1 = 1$

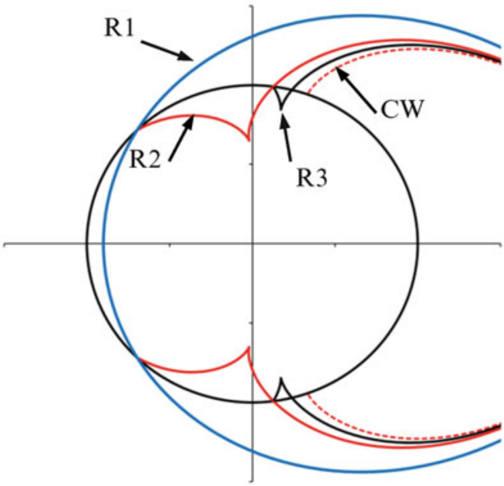

Fig. 24 Interaction with a fluid-filled cylindrical shell. Sonic case: $d/R = 3.9$, $c_2/c_1 = 1$. First three reflected wave fronts (R1: *blue*, R2: *red*, R3: *black*) and CW front (*dashed red line*) when

In Fig. 28, the line AF is extended until F reaches the inside of the shell. That is, until $AF = 2\cos(i_2)$. It shows that direct rays do not reach the entire volume inside the shell and they also form a caustic in the upper right quadrant. This results in direct wave fronts that do not reach the shell when $d/R > 0.8990$ and in some cases cusp singularities occur on the caustic. When $d/R = 4.21$ this wave front is singular since it reaches the caustic. The DWI start reflecting from the inside surface when $d/R > 2\,c_1/c_2 = 4.651$. We also note that these wave fronts all start on the ray emanating from the tangent point T1 in Fig. 12.

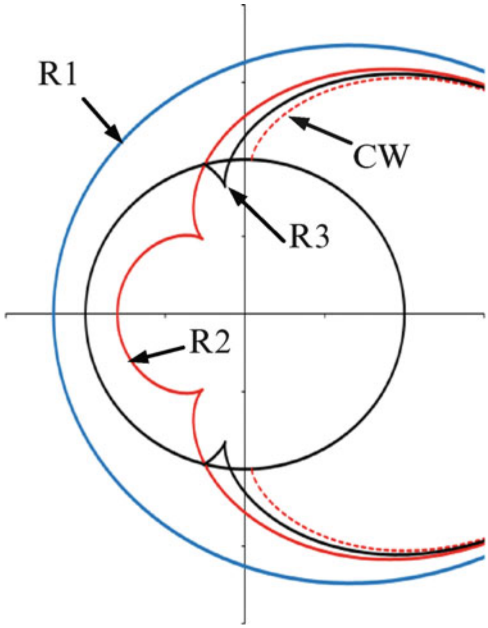

Fig. 25 Interaction with a fluid-filled cylindrical shell. Sonic case: d/R = 4.20, $c_2/c_1 = 1$. First three reflected wave fronts (R1: *blue*, R2: *red*, R3: *black*) and CW front (*dashed red line*)

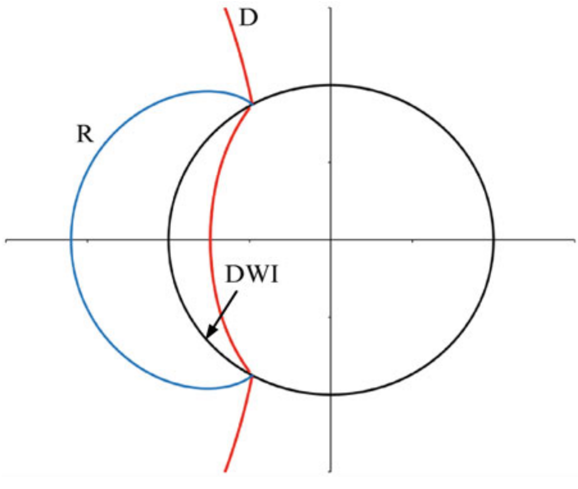

Fig. 26 Interaction with a fluid-filled cylindrical shell. Subsonic case: d/R = 0.6, $c_2/c_1 = 0.43$

The creeping wave propagating around the outside circumference of the shell has a 90° angle of incidence relative to the radial direction. According to Snell's law this wave is transmitted to the inside fluid at an angle given by

$$i_2 = \sin^{-1}(c_2/c_1)$$

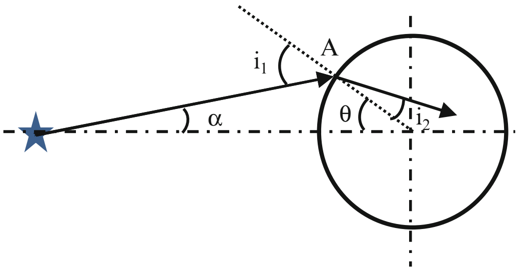

Fig. 27 Ray tracing procedure for direct wave inside when $c_2/c_1 \neq 1$

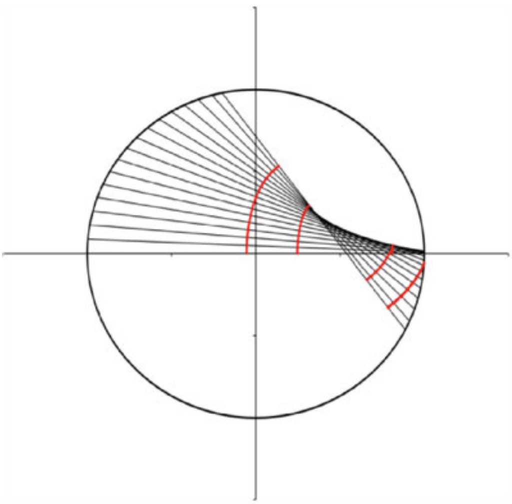

Fig. 28 Interaction with a fluid-filled cylindrical shell. Subsonic case: $c_2/c_1 = 0.43$. Direct rays inside the shell and corresponding wave fronts for d/R = 2.2, 2.9, 4.21, and 4.7

In the present example, $c_2/c_1 = 0.43$ so $i_2 = 25.5°$. Figure 29 shows that a ray from the source S to the tangent point T1, followed by a creeping wave from T1 to an arbitrary point P on the circumference is followed by a ray PG in the inside fluid. The total length ST1 + T1P + PG.c2/c1 is equal to the radius of the direct wave in the outside fluid. The wave front generated by this creeping wave after it is transmitted to the inside fluid is labeled CWI. This CWI wave front connects smoothly to the DWI (Fig. 30).

Rays generating the CWI wave front make an angle $i_2 = \sin^{-1}(c_2/c_1)$ with the radial direction. Their envelope is the circle of radius Rc_2/c_1 shown in Fig. 31. The dashed line in that figure starts from the tangent point T1 and makes an angle i_2 with the radial direction. It can be shown that the CWI wave front starts on the line AB when $0.89890 < d/R < 5.0982$. That wave front is smooth when $0.89890 < d/R < 2.9986$ and becomes singular when $2.9986 < d/R < 5.0982$ as shown in Fig. 31.

When d/R = 2.9, the top and bottom creeping wave fronts cross each other as they circumvent the shell on the outside, and same occurs for the CWI wave

Fig. 29 Interaction with a fluid-filled cylindrical shell. Subsonic case. Ray tracing procedure for creeping waves inside (CWI)

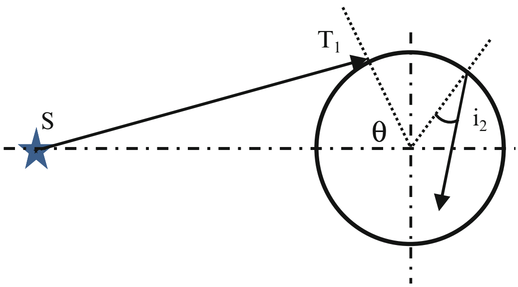

Fig. 30 Interaction with a fluid-filled cylindrical shell. Subsonic case: $d/R = 2.2$, $c_2/c_1 = 0.43$

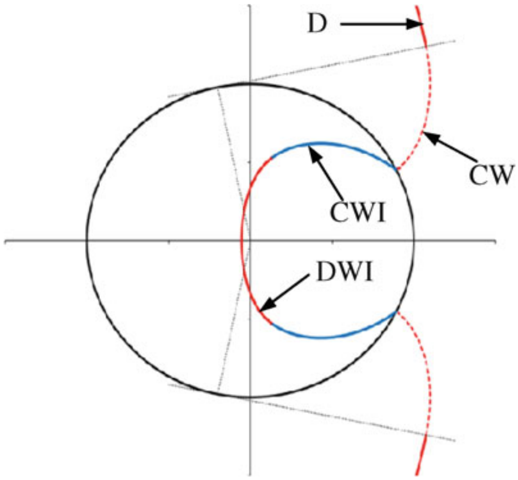

Fig. 31 Interaction with a fluid-filled cylindrical shell. Subsonic case: $c_2/c_1 = 0.43$. CWI wave fronts and related caustic

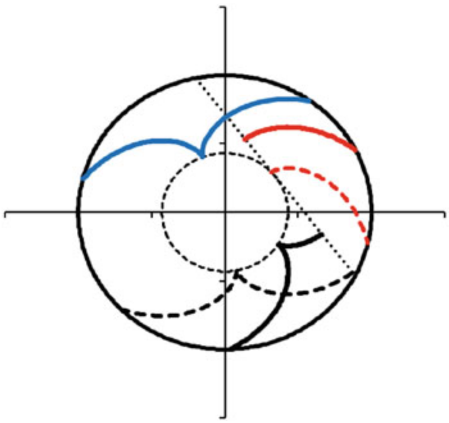

fronts inside the shell (Fig. 32). $d/R = 4.21$ both DWI and CWI wave fronts have cusp singularities (Fig. 33) as already indicated in Figs. 28 and 31. After a single reflection from the inside of the shell, rays form the pattern shown in Fig. 34 where it can be seen that the wave fronts are restricted to a small region and that a caustic is formed in the lower left quadrant.

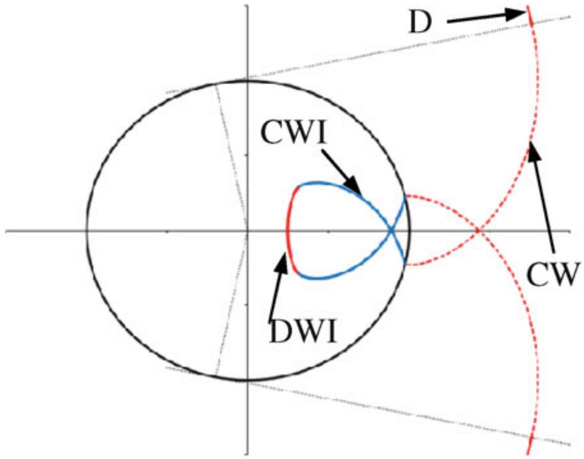

Fig. 32 Interaction with a fluid-filled cylindrical shell. Subsonic case: $d/R = 2.9$, $c_2/c_1 = 0.43$

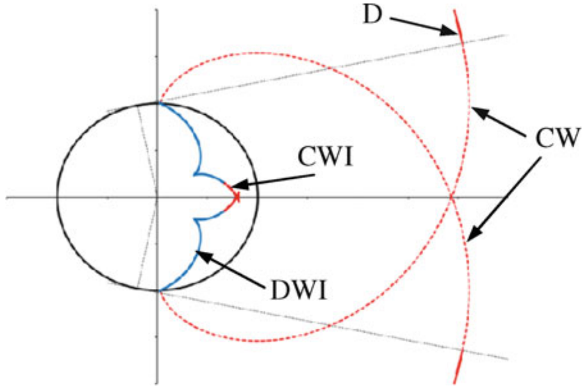

Fig. 33 Interaction with a fluid-filled cylindrical shell. Subsonic case: $d/R = 4.21$, $c_2/c_1 = 0.43$

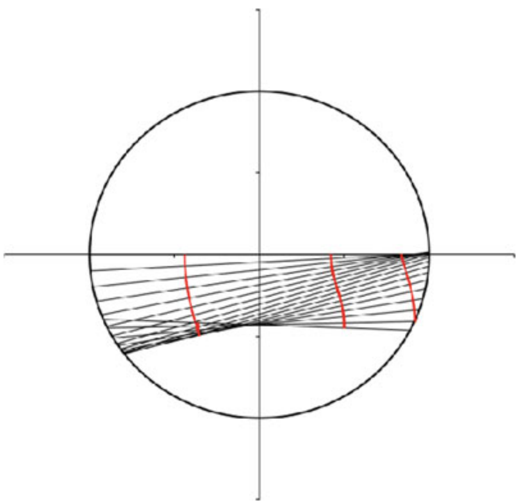

Fig. 34 Interaction with a fluid-filled cylindrical shell. Subsonic case: $c_2/c_1 = 0.43$. R1 caustic and wave fronts for several values of d/R

Fig. 35 Interaction with a fluid-filled cylindrical shell. Subsonic case: d/R = 6, $c_2/c_1 = 0.43$

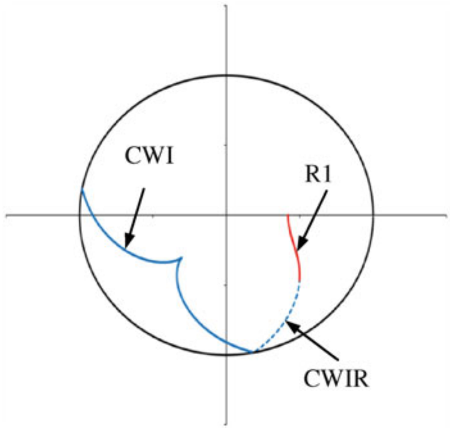

Fig. 36 Interaction with a fluid-filled cylindrical shell. Subsonic case: d/R = 8, $c_2/c_1 = 0.43$

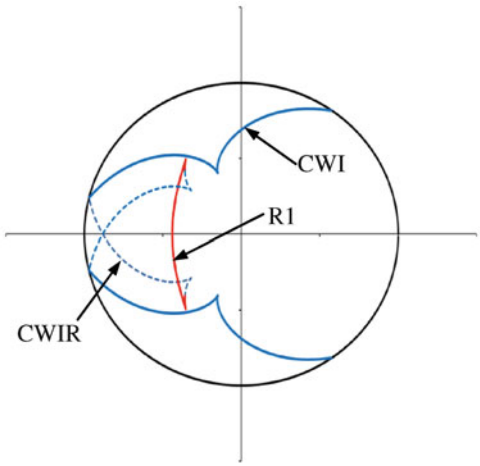

When d/R = 6 we notice three types of wave fronts (Fig. 35): the CWI wave front, the portion of the CWI wave front that is reflected from the inside surface of the shell, and the R1 wave front previously shown in Fig. 34. Figure 35 only shows wave fronts generated by initial rays starting above the horizontal axis. Initial rays below that axis generate three more wave fronts that are mirror images of those shown on the figure. They are not shown in order to keep the figure simple. On the other hand, Fig. 36 shows both sets wave fronts are drawn for d/R = 8. In this case the reflected CWI wave fronts also have a singularity and they cross along the horizontal axis. The R1 wave front also has a singularity as indicated in Fig. 34 and it meets the CWI wave front at that singular point.

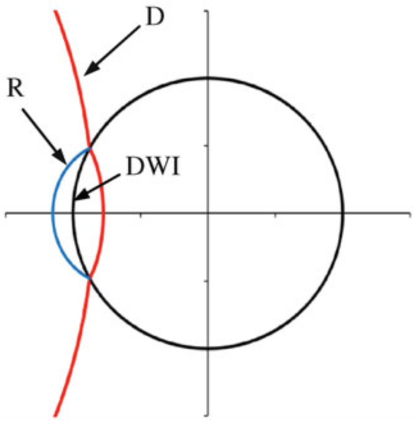

Fig. 37 Interaction with a fluid-filled cylindrical shell. Supersonic case: $d/R = 0.15$, $c_2/c_1 = 1.5$

5.5 Interaction of a Cylindrical Wave with a Fluid-Filled Shell: Supersonic Case

A different behavior is observed when the speed of sound is higher inside the shell than outside ($c_2/c_1 > 1$). In this example, $c_2/c_1 = 1.5$. The main result is that rays traveling though the inside fluid generate new wave fronts in the outside fluid.

First, using the construction shown in Fig. 27, we find that the refracted angle $i_2 = 90°$ when the incident angle $i_1 = 41.8°$ and that occurs when $\theta = 34.15°$ and $d/R = 0.2100$. When $d/R < 0.21$, wave fronts for the direct wave outside and the direct wave inside meet as they both reach the shell as shown in Fig. 37 when $d/R = 0.15$. Waves propagate faster inside the shell. When $d/R > 0.21$, the two wavefronts (DWO and DWI) no longer meet along the circumference of the shell as shown in Fig. 38 for $d/R = 0.6$. We find that, for this particular example ($D/R = 5$, $d/R = 0.6$), when $32.045° < \theta < 34.15°$ refracted rays reach the inside of the shell and generate refracted rays in the inside fluid and transmitted rays outside (Fig. 37). The incident ray SA makes an angle i_1 with the radial direction while AB makes an angle i_2 with that direction. At B, the reflected ray BC makes an angle i_2 with the radial direction while the transmitted ray BD is at an angle i_1. Snell's law relates the angle i_2 to i_1. When $\theta = 34.15°$, the transmitted wave front meets the reflected wave front on a line making a 41.8° angle with the radial direction at point A.

Figure 38 shows another wave front for rays traveling through the inside fluid and out into the outside fluid but the R1 reflected front is too small to be clearly visible (Fig. 39). However it is clearly visible when $d/R = 1.0$ (Fig. 40). The IO wave front is seen to start from where the R1 wave front starts and it joins smoothly with the reflected wave front R. When $d/R = 1.4$ the direct rays have all reached the back of the shell and have reflected to give a R1 wave front inside and in the outside fluid the two IO fronts shown in Figs. 38 and 40 merged together (Fig. 41).

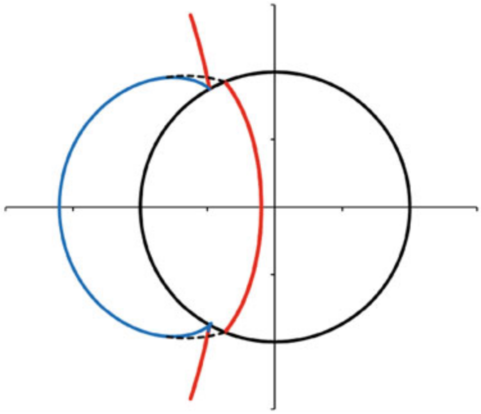

Fig. 38 Interaction with a fluid-filled cylindrical shell. Supersonic case: d/R = 0.6, $c_2/c_1 = 1.5$

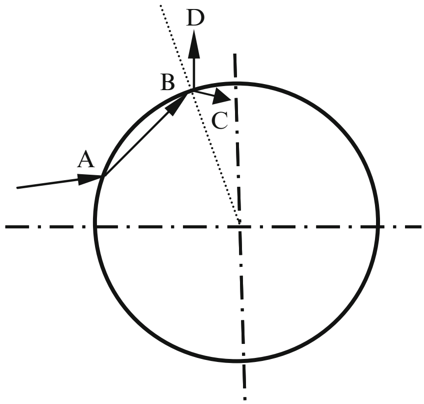

Fig. 39 Construction of transmitted wave front (T) and reflected wave front R1 for supersonic case

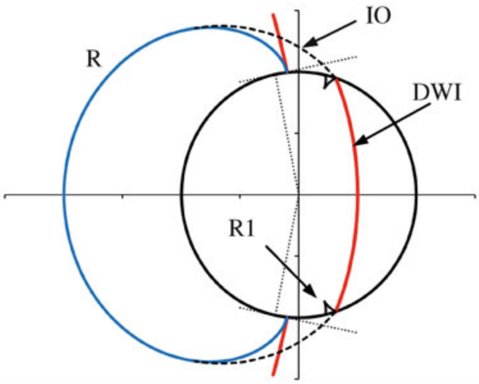

Fig. 40 Interaction with a fluid-filled cylindrical shell. Supersonic case: d/R = 1.0, $c_2/c_1 = 1.5$

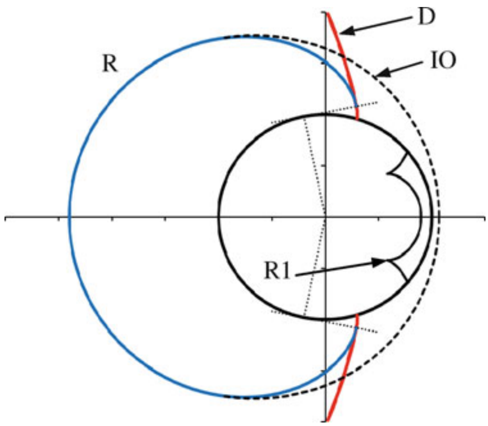

Fig. 41 Interaction with a fluid-filled cylindrical shell. Supersonic case: d/R = 1.4, $c_2/c_1 = 1.5$

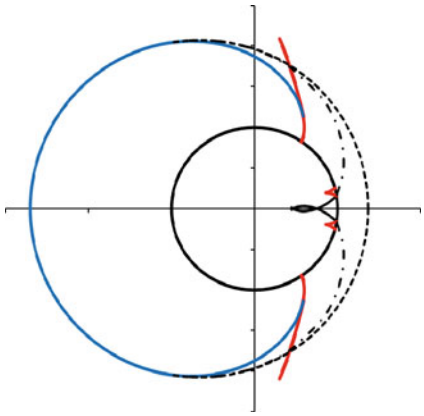

Fig. 42 Interaction with a fluid-filled cylindrical shell. Supersonic case: d/R = 1.7, $c_2/c_1 = 1.5$

For d/R = 1.7, R_2 wave fronts corresponding to two reflections from the inside of the shell are seen in the inside fluid (Fig. 42). A second wave front labeled IO2 initiates from the start of the R2 front and then joins smoothly with the IO front. When d/R = 2.4, the same pattern is observed (Fig. 43) and in addition we see a third IO front starting from the end the R2 wave front inside. The end of R2 is also the beginning of R3 which is not shown on the figure because it is too small. In Fig. 43, the R1 front does not have a singularity. Results in Figs. 38, 40, 41, 42 and 43 are in good agreement with those shown in Fig. 9 of Iakovlev [145].

The evolution of the shape and size of the R1 wave fronts can be seen in Fig. 44. When d/R = 1.0, 1.4, and 1.7 the wave front has a singularity when it reaches the caustic formed by the reflected rays. For d/R = 2.4, the R1 front is smooth.

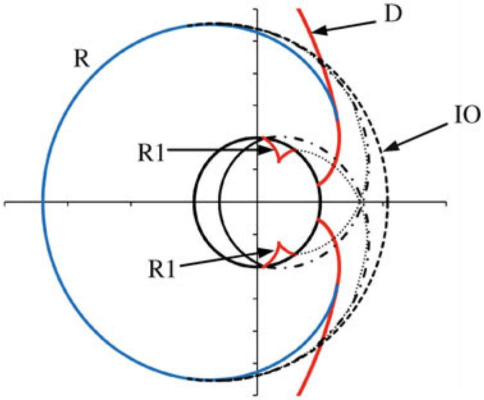

Fig. 43 Interaction with a fluid-filled cylindrical shell. Supersonic case: $d/R = 2.4$, $c_2/c_1 = 1.5$

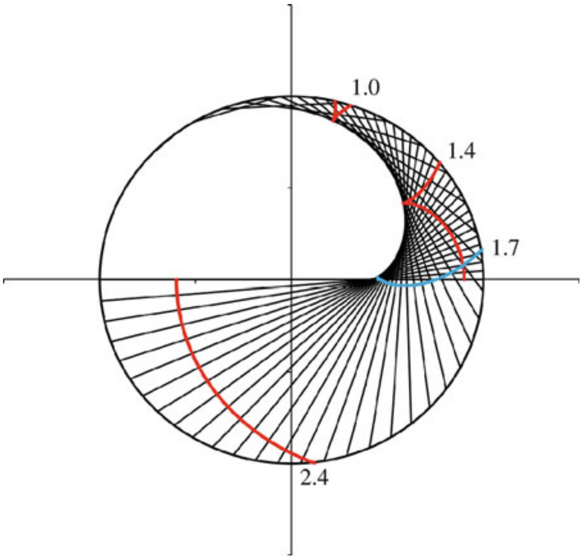

Fig. 44 Rays after one reflection from the inside of the shell, caustic, and wave fronts for several values of d/R, $c_2/c_1 = 1.5$

6 Related Problems

The approach developed to study shock wave interactions with submerged structures can be applied to other areas. This section describes how it can be applied to better understand a commonly used medical procedure called lithotripsy and to understand the development of traumatic brain injury (TBI) caused by impacts and explosions.

6.1 Lithotripsy

Shock wave lithotripsy (SWL) is a noninvasive procedure for kidney stone removal that was introduced in the United States in 1984. An overview of SWL is given by Bailey et al. [165, 166]. The device used for this procedure is called a extracorporeal shock wave lithotripter and it has three main components, a shock wave source, a method of acoustically coupling shock waves to the patient, and an imaging system for targeting. Lithotripters produce decaying pulses that can be described by the expression introduced by Friedlander for explosions in air

$$p = p_o \left(1 - \frac{t}{t_o}\right) e^{-\alpha\, t/t_o} \tag{66}$$

where t_o is the duration of the positive phase, p_o is the maximum pressure, and α indirectly defines the magnitude of the negative phase. Typically, a positive pressure spike with a duration of 1 μs followed by a 5 μs duration, negative pressure trough. Peak positive amplitudes range from 15 to 150 MPa and negative pressures are in the −8 to −15 MPa range. Typically, 2,000–4,000 shock waves are administered at a rate between 0.5 and 2 Hz. With this procedure, the shock waves break up the kidney stones.

Dahake et al. [167, 168] studied the interaction of shock waves with 22 mm cylinder made out of plaster immersed in water. Plaster is used to simulate kidney stones and, in that material, longitudinal waves propagates with velocity $c_L = 3.3$ mm/μs and shear waves with $c_s = 1.75$ mm/μs. The speed of sound in water is $c_w = 1.5$ mm/μs. Using the method developed in the present study we consider a source located 90 mm to the left of the cylinder.

Figure 45a shows the position of the shock wave in the water 6 μs after it has reached the cylinder. Inside the solid cylinder waves propagate faster than in the water and Fig. 45 shows four wave fronts inside. As a ray reaches the surface of the water it generates both a compressional wave PP and a shear wave PS in the cylinder (Fig. 45b). Some PP rays reach the surface of the cylinder and are reflected generating a PPP wave and PPS wave (Fig. 45c, d).

As the PP rays reach the surface of the cylinder, the reflected rays form a caustic (Fig. 46). The PPP wave front has a fold type singularity and that singularity occurs on the caustic.

After 8 μs, the PP wave front disappears and the PPP and PPS wave front have changed shape as shown in Fig. 47. The PPs wave front becomes singular as it reaches its caustic (Fig. 48).

The present approach gives precise prediction for the position of the various wave fronts which is difficult to obtain using numerical approaches such as the finite difference method used by Dahake et al. [168] for example. Several other authors have studied the propagation of shock waves in kidney stones [169–171].

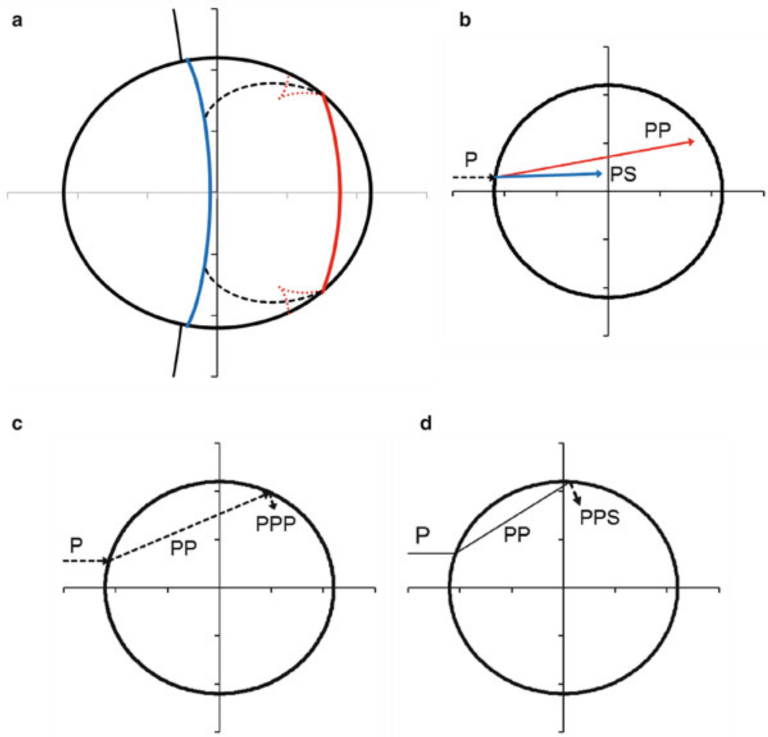

Fig. 45 Lithotripsy. Interaction of water borne shock wave with a plaster cylinder. (**a**) wave fronts for t = 6 μs; (**b**) Ray tracing procedure for the direct compression (*PP*) and shear wave (*PS*) fronts; (**c**) Ray tracing procedure for the PPP front; (d) Ray tracing procedure for the PPS front

6.2 Traumatic Brain Injury

Many articles have been devoted to the study of impacts on the human head. Young [172] modeled the head as a spherical fluid-filled shell. In the impact model, the head makes contact with a surface though a nonlinear spring representing the local deformation according to Hertz's contact law. That nonlinear spring acts in series with a linear spring that accounts for the deformation of the shell. Using this model, closed form solutions were obtained for the impact duration and the maximum impact force. The response of the fluid inside the shell is expected to remain hydrostatic if the duration of the impact is larger than 4 times the period of the first n = 2 spheroidal mode of the shell [172]. Analyses of the natural frequencies and mode shapes of fluid-filled spherical shells are found in [173–175].

A simple analysis for understanding the propagation of waves through the brain is provided by Babbs [176, 177]. In this model, an elastic bar is impacting a rigid surface with an initial velocity. Elastic waves propagate along the bar, reflect from the free end and return towards the impact point. The dynamic response

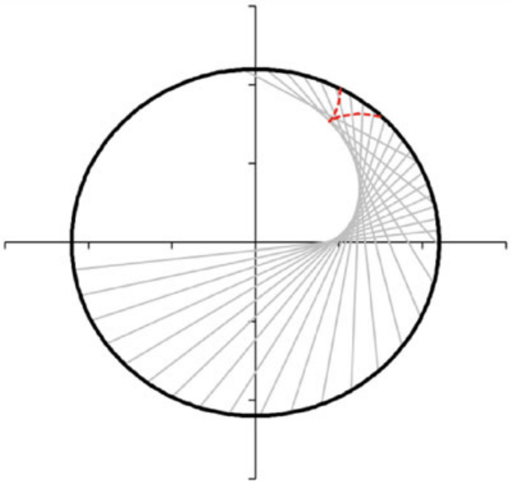

Fig. 46 Lithotripsy. Interaction of water borne shock wave with a plaster cylinder. 6 μs

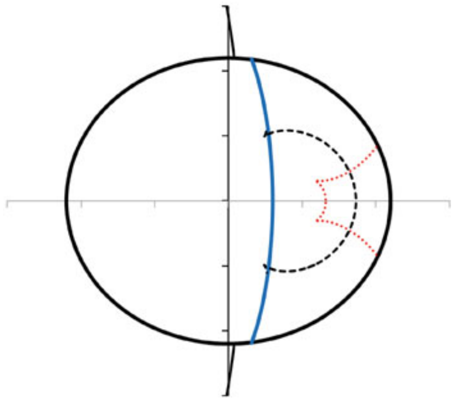

Fig. 47 Lithotripsy. Interaction of water borne shock wave with a plaster cylinder. The PS, PPP, and PPS wave fronts 8 μs after the shock wave has reached the cylinder

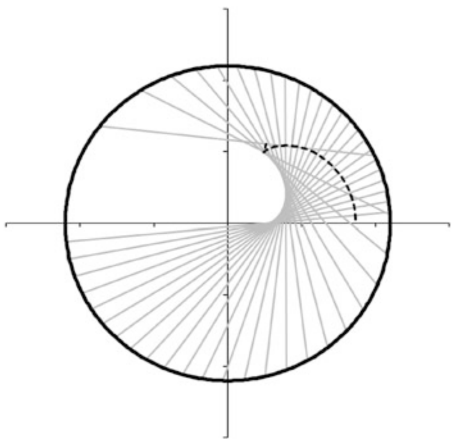

Fig. 48 Lithotripsy. Interaction of water borne shock wave with a plaster cylinder. Caustic and PPS wave front for t = 8 μs

of a fluid-filled spherical shell subjected to a radial impulsive load was studied analytically by Engin [178] in order to predict both skull fracture and brain damage. This model was extended by Kenner and Goldsmith [179, 180]. Finite element models of a human head subject to an impact force were developed by many authors including Engin et al. [181] who produced many contour plots for pressure levels inside the brain at different times.

A number of studies [e.g. 182, 183] used numerical simulations to study the role of blast wave interactions with the human head in producing traumatic brain injury. Grujicic et al [184] used a six layer one-dimensional model to simulate the effect of blasts on the head of a soldier wearing a helmet with polyurea suspension pads. The six layers are: a layer of air, a Kevlar-phenolic layer representing the helmet shell, a layer of polyurea, the skull, the cerebro-spinal fluid and the cerebrum. The objective is to assess the ability of polyurea to mitigate the effects of blast loading and, in turn, to reduce the possibility for TBI. A full three-dimensional analysis of this problem [185] showed the propagation of waves through the brain and through the skull at a faster speed. Simulations of blast waves with human head wearing a helmet can also be found in [186].

7 Conclusion

This chapter presented an overview of the physics of underwater explosions and wave propagation in solids and along fluid–structure interfaces. A geometrical approach is used to study the shock wave interactions with submerged structures and predict the position of wave fronts as a function of time. This simple approach gives a whole field view of these interactions and brings insights that are difficult to gain from numerical simulations. Several examples are presented for interactions with fluid-filled cylindrical shells and the method accurately predicted the evolution of complex patterns with many wave fronts. Singularities in some wave fronts were explained in terms of caustics formed by the rays generating these wave fronts. Singularities occur when the wave front reaches the caustic and singular points are located on the caustic. The method is shown to apply to other problems in the medical field.

Acknowledgements This work was supported by grant from the Office of Naval Research. The advice and encouragement of the program manager Dr. Y.D.S. Rajapakse are greatly appreciated.

References

1. Cole RH (1948) Underwater explosions. Princeton University Press, Princeton
2. Pritchett JW (1971) An evaluation of various theoretical models for underwater explosion bubbles. DTIC report AD Number: AD0737271
3. Hunter KS, Geers TL (2004) Pressure and velocity fields produced by an underwater explosion. J Acoust Soc Am 115(4):1483–1496

4. Arons AB (1954) Underwater explosion shock wave parameters at large distances from the charge. J Acoust Soc Am 26(3):343–346
5. Murata K, Takahashi K, Kato Y (1999) Precise measurements of underwater explosion phenomena by pressure sensor using fluoropolymer. J Mater Process Technol 85(1–3): 39–42
6. Kalavalapally R, Penmetsa R, Grandhi R (2006) Multidisciplinary optimization of a lightweight torpedo structure subjected to an underwater explosion. Finite Elem Anal Des 43:103–111
7. Kalavalapally R, Penmetsa R, Grandhi R (2009) Configuration design of a lightweight torpedo subjected to an underwater explosion. Int J Impact Eng 36:343–351
8. Van Der Schaaf P (1992) Underwater shock in the far-field from a distribution of charges. DTIC report Number ADA253458
9. Reid WD (1996) The response of surface ships to underwater explosions. Report DSTO-GD-0109
10. Arons AB, Slifko JP, Carter A (1948) Secondary pressure pulses due to gas globe oscillation in underwater explosions I. Experimental data. J Acoust Soc Am 20(3):271–276
11. Chapman NR (1988) Source levels of shallow explosive charges. J Acoust Soc Am 84(2): 697–702
12. Klaseboer E, Khoo BC, Hun KC (2005) Dynamics of an oscillating bubble near a floating structure. J Fluid Struct 21(4):395–412
13. Wang C, Khoo BC (2004) An indirect boundary element method for three-dimensional explosion bubbles. J Comput Phys 194(2–4):451–480
14. Zhang AM, Yao XL, Yu XB (2008) The dynamics of three-dimensional underwater explosion bubble. J Sound Vib 311(3–5):1196–1212
15. Vernon TA (1986) Whipping response of ship hulls from underwater explosion bubble loading. Technical memorandum 86/255, Defence Research Establishment Atlantic, pp 1–41
16. Snay HG (1962) Underwater explosion phenomena: the parameters of migrating bubbles. Technical report NAVORD 4185, U.S. Naval Ordnance Laboratory, White Oak, MD
17. Leybourne AE (1990) An extension of underwater explosive models to include the high frequency transients following pulse maxima. Math Comput Model 14:771–775
18. Reid WD (1996) The response of surface ships to underwater explosions. DSTO report DSTO-GD-0109
19. Lee M, Klaseboer E, Khoo BC (2007) On the boundary integral method for the rebounding bubble. J Fluid Mech 570:407–429
20. Rayleigh JW (1917) On the pressure developed in a liquid during the collapse of a spherical cavity. Philos Mag 34(3):94–98
21. Willis HF (1941) Underwater explosions: the time interval between successive explosions. British Report, WA-42-21
22. Chahine GL (1977) Interaction between an oscillating bubble and a free surface. J Fluids Eng Ser I 99:709–716
23. Lamb H (1923) The early stages of a submarine explosion. Philos Mag 45:257–265
24. Afanasiev KE, Grigorieva IV (2006) Numerical investigation of three-dimensional bubble dynamics. J Eng Math 55:65–80
25. Best JP (2002) The effect of non-spherical collapse on determination of explosion bubble parameters. DSTO report DSTO-RR-0238
26. Best JP, Kucera A (1992) A numerical investigation of non-spherical rebounding bubbles. J Fluid Mech 245:137–154
27. Klaseboer E, Khoo BC (2006) A modified Rayleigh-Plesset model for a non-spherically symmetric oscillating bubble with applications to boundary integral methods. Eng Anal Bound Elem 30(1):59–71
28. Keller JB (1980) Some bubble and contact problems. SIAM Rev 22(4):442–458
29. Keller JB, Kolodner II (1956) Damping of underwater explosion bubble oscillations. J Appl Phys 27:1152–1161
30. Geers TL, Park CK (2005) Optimization of the G&H bubble model. Shock Vib 12(1):3–8

31. Beshara FBA (1994) Modelling of blast loading on aboveground structures—I. General phenomenology and external blast. Comput Struct 51(5):585–596
32. Krauthammer T (2008) Modern protective structures. CRC Press, Boca Raton
33. Achenbach JD (1973) Wave propagation in elastic solids. North-Holland, Amsterdam
34. Ewing EW (1957) Elastic waves in layered media. McGraw-Hill, New York
35. Graff KF (1975) Wave motion in elastic solids. Ohio State University, Columbus
36. Miklowitz J (1978) The theory of elastic waves and waveguides. North Holland Pub. Co., Amsterdam
37. Brekhovskikh LM (1980) Waves in layered media. Academic Press, New York
38. Viktorov IA (1967) Rayleigh and lamb waves. Plenum Press, New York
39. Lighthill J (2001) Waves in fluids. Cambridge University Press, Cambridge
40. Whitham GB (1974) Linear and nonlinear waves. Wiley, New York
41. Brekhovskikh LM, Lysanov IP (2003) Fundamentals of ocean acoustics, AIP series in modern acoustics and signal processing. Springer, New York
42. Rayleigh JW (1889) On the free vibrations of an infinite plate of homogeneous isotropic elastic matter. Proc Lond Math Soc 1–20:225–234
43. Jagnoux P, Vincent A (1989) Ultrasonic imaging by leaky Rayleigh waves. NDT Int 22(6):329–346
44. Royer D, Clorennec D (2007) An improved approximation for the Rayleigh wave equation. Ultrasonics 46:23–24
45. Li XF (2006) On approximate analytic expressions for the velocity of Rayleigh waves. Wave Motion 44:120–127
46. Nkemzi DW (2008) A simple and explicit algebraic expression for the Rayleigh wave velocity. Mech Res Commun 35(3):201–205
47. Nkemzi DW (1997) A new formula for the velocity of Rayleigh waves. Wave Motion 26(2):199–205
48. Ogden RW, Vinh PC (2004) On Rayleigh waves in incompressible orthotropic elastic solids. J Acous Soc Am 115(2):530–533
49. Vinh PC (2010) On formulas for the velocity of Rayleigh waves in prestrained incompressible elastic solids. J Appl Mech 77(2):1–9, Article Number: 021006
50. Vinh PC, Giang PTH (2010) On formulas for the Rayleigh wave velocity in pre-strained elastic materials subject to an isotropic internal constraint. Int J Eng Sci 48(3):275–289
51. Rahmana M, Michelitsch T (2006) A note on the formula for the Rayleigh wave speed. Wave Motion 43:272–276
52. Vinh PC, Malischewsky PG (2008) Improved approximations of the Rayleigh wave velocity. J Thermoplast Comp Mate 21(4):337–352
53. Vinh PC, Malischewsky PG (2007) An improved approximation of Bergmann's form for the Rayleigh wave velocity. Ultrasonics 47(1–4):49–54
54. Vinh PC, Malischewsky PG (2007) An approach for obtaining approximate formulas for the Rayleigh wave velocity. Wave Motion 44(7–8):549–562
55. Vinh PC, Malischewsky PG (2006) Explanation for Malischewsky's approximate expression for the Rayleigh wave velocity. Ultrasonics 45(1–4):77–81
56. Vinh PC, Ogden RW (2004) On formulas for the Rayleigh wave speed. Wave Motion 39(3):191–197
57. Vinh PC, Ogden RW (2004) Formulas for the Rayleigh wave speed in orthotropic elastic solids. Arch Mech 56(3):247–265
58. Vinh PC, Ogden RW (2005) On the Rayleigh wave speed in orthotropic elastic solids. Meccanica 40(2):147–161
59. Neuenschwander J, Schmidt T, Luthi T, Romer M (2006) Leaky Rayleigh wave investigation on mortar samples. Ultrasonics 45:50–55
60. Goodman RR, Bunney RE, Marshall SW (1967) Observation of circumferential waves on solid aluminum cylinders. J Acoust Soc Am 42:523–524
61. Szilard J (1982) Ultrasonic testing—non-conventional testing techniques. Wiley, New York

62. Jin F, Wang Z, Kishimoto K (2005) Basic properties of Rayleigh surface wave propagation along curved surfaces. Int J Eng Sci 43(3–4):250–261
63. Bunney RE, Goodman RR, Marshall SW (1969) Rayleigh and lamb waves on cylinders. J Acoust Soc Am 46(5b):1223–1233
64. Lamb H (1917) On waves in an elastic plate. Proc R Soc Lond Seri A 93(648):114–128
65. Osborne MFM, Hart SD (1945) Transmission, reflection, and guiding of an exponential pulse by a steel plate in water. I. Theory. J Acoust Soc Am 17(1):1–18
66. Uberall H, Ahyi AC, Raju PK, Bjorno IK, Bjorno L (2002) Circumferential-wave phase velocities for empty, fluid-immersed spherical metal shells. J Acoust Soc Am 112(6): 2713–2720
67. Uberall H, Bjorno IK, Bjorno L (2000) Dispersion of circumferential waves on evacuated, water-loaded spherical steel shells. Ultrasonics 37(10):673–675
68. Cheeke JDN, Li X, Wang Z (1998) Observation of flexural lamb waves (Ao mode) on water-filled cylindrical shells. J Acoust Soc Am 104(6):3678–3680
69. Stoneley R (1924) Elastic waves at the surface of separation of two solids. Proc R Soc Lond Ser A 106:416–420
70. Scholte JGJ (1956) On seismic waves in a spherical earth. Koninklijk Nederlands Meteorologisch Instituut, Commun, No. 65, The Hague, pp 1–55
71. Jenot F, Ouaftouh M, Duquennoy M, Ourak M (2005) Interferometric detection of acoustic waves at air-solid interface. Applications to non-destructive testing. J Appl Phys 97, 094905
72. Kaufman AA, Levshin AL (2005) Acoustic and elastic wave fields in geophysics, vol 3. Elsevier, ISBN 04445 19556, 97804445 19559
73. Meegan GD, Hamilton MF, Il''inskii YA, Zabolotskaya EA (1999) Nonlinear Stoneley and Scholte waves. J Acoust Soc Am 106:1712–1723
74. Glorieux C, Van de Rostyne K, Nelson K, Gao W, Lauriks W, Thoen J (2001) On the character of acoustic waves at the interface between hard and soft solids and liquids. J Acoust Soc Am 110(3), Pt. 1, 1299–1308
75. Weng X, Yew CH (1990) The leaky Rayleigh wave and Scholte wave at the interface between water and porous sea ice. J Acoust Soc Am 87(6):2481–2488
76. Uberall H (2001) Acoustics of shells. Acoust Phys 47(2):115–139
77. Bao XL, Franklin H, Raju PK, Überall H (1997) The splitting of dispersion curves for plates fluid-loaded on both sides. J Acoust Soc Am 102(2):1246–1248
78. Sessarego J-P, Sageloli J, Gazanhes C, Uberall H (1997) Two Scholte–Stoneley waves on doubly fluid-loaded plates and shells. J Acoust Soc Am 101(1):135–142
79. Bao XL, Raju PK, Überall H (1999) Circumferential waves on an immersed, fluid-filled elastic cylindrical shell. J Acoust Soc Am 105(5):2704–2709
80. Kim JY, Ih JG (2003) Scattering of plane acoustic waves by a transversely isotropic cylindrical shell – application to material characterization. Appl Acoust 64(12):1187–1204
81. Maze G, Leon F, Ripoche J et al (1995) Nature of Scholte interface waves on cylindrical-shells. Acustica 81(3):201–213
82. Maze G, Léon F, Ripoche J, Überall H (1999) Repulsion phenomena in the phase-velocity dispersion curves of circumferential waves on elastic cylindrical shells. J Acoust Soc Am 105(3):1695–1701
83. Franz W (1954) Uber die Greenschen Functionen des Zylinderus und der Kugel. Z. Naturforsch 9A, 705–716
84. Barnard GR, McKinney CM (1961) Scattering of acoustic energy by solid and air-filled cylinders in water. J Acoust Soc Am 33(2):226–238
85. Neubauer WG (1968) Experimental measurement of "creeping" waves on solid aluminum cylinders in water using pulses. J Acoust Soc Am 44(1):298–299
86. Neubauer WG (1968) Experimental observation of three types of pulsed circumferential waves on solid aluminum cylinders. J Acoust Soc Am 44(4):1150–1152
87. Ahyi AC, Pernod P, Gatti O et al (1998) Experimental demonstration of the pseudo-Rayleigh (A(0)) wave. J Acoust Soc Am 104(5):2727–2732

88. Latard V, Merlen A, Preobazhenski V, Ahyi AC (1999) Acoustic scattering of impulsive geometrical waves by a glass sphere in water. Appl Phys Lett 74(13):1919–1921
89. Neubauer WG (1969) Pulsed circumferential waves on aluminum cylinders in water. J Acoust Soc Am 45(5):1134–1144
90. Überall H, Doolittle RD, McNicholas JV (1966) Use of sound pulses for a study of circumferential waves. J Acoust Soc Am 39(3):564–578
91. Ugincius P (1968) Creeping-wave analysis of acoustic scattering by elastic cylindrical shells. NWL technical report TR-2128
92. Ugincius P, Oberall H (1968) Creeping wave analysis of acoustic scattering by elastic cylindrical shells. J Acoust Soc Am 58(1025–1035):1968
93. Nguyen XN, Dahm T, Grevemeyer I (2009) Inversion of Scholte wave dispersion and waveform modeling for shallow structure of the ninetyeast ridge. J Seismol 13(4):543–559
94. Stoll RD, Bautista EO, Akal T (1996) Generating interface waves using a freely falling, instrumented source. IEEE J Oceanic Eng 21(4):452–457
95. Kotenkoff C, Lacoume JL, Mars M (2005) Multicomponent seismo-acoustic surface waves beamforming for undersea buried object detection. Oceans 2005 Europe International Conference, Brest, France, June 20–23, 2005. Oceans 2005 – Europe, vols 1 and 2, pp 769–774
96. Lefevre F, Jenot F, Ouaftouh M, et al (2010) Laser generated guided waves and finite element modeling for the thickness gauging of thin layers. Rev Sci Instrum 81(3), Article Number: 034901
97. Jenot F, Ouaftouh M, Duquennoy M et al (2005) Sizing of structures by laser ultrasonics using air-solid interface waves. Rev Prog Quant Nondestruct Eval 760:305–312
98. Su Z, Ye L (2009) Identification of damage using lamb waves: from fundamentals to applications. Springer, London
99. Zhu JY, Popovics JS, Schubert F (2004) Leaky Rayleigh and Scholte waves at the fluid–solid interface subjected to transient point loading. J Acoust Soc Am 116(4):2101–2110
100. Zhu JY, Popovics JS (2006) Analytical study of excitation and measurement of fluid–solid interface waves. Geophys Res Lett 33(9), Article Number: L09603
101. Luke BA, Stokoe KH (1998) Application of SASW method underwater. J Geotech Geoenviron Eng 124(6):523–531
102. Herber R, Grevemeyer I, Exner O et al (1998) An implosive seismoacoustic source for seismic experiments on the ocean floor. Mar Geophys Res 20(3):239–247
103. Fu D, Liu L, Chen Y, Zhu G (2001) Phase difference and interference between reflected cylindrical wave and head wave at a liquid/solid interface. Chin Sci Bull 46(18):1556–1560
104. Alkier KW (1978) Underwater acoustic backscattering and echo structure characteristics for a thin stiffened plate. J Acoust Soc Am 63(3):704–708
105. Bingham J, Hinders M, Friedman A (2009) Lamb wave detection of limpet mines on ship hulls. Ultrasonics 49(8):706–722
106. Wardlaw AB, Luton JA (2000) Fluid–structure interaction mechanisms for close-in explosions. Shock Vib 7(5):265–275
107. Xie WF, Young YL, Liu TG et al (2007) Dynamic response of deformable structures subjected to shock load and cavitation reload. Comput Mech 40(4):667–681
108. Young YL, Liu Z, Xie W (2009) Fluid–structure and shock-bubble interaction effects during underwater explosions near composite structures. J Appl Mech 76(5):1–10
109. Xie W, Liu Z, Young YL (2009) Application of a coupled Eulerian–Lagrangian method to simulate interactions between deformable composite structures and compressible multiphase flow. Int J Numerical Methods Eng 80(12):1497–1519
110. Liu Z, Young YL, Motley MR (2010) Transient response of partially-bonded sandwich plates subject to underwater explosions. Shock Vib 17(3):233–250
111. Xie WF, Young YL, Liu TG (2008) Multiphase modeling of dynamic fluid–structure interaction during close-in explosion. Int J Numer Methods Eng 74(6):1019–1043
112. Fleck NA, Deshpande VS (2004) The resistance of clamped sandwich beams to shock loading. J Appl Mech 71(3):386–401

113. Pan YG, Watson A (1998) Effect of panel stiffness on resistance of cladding panels to blast loading. J Eng Mech 124(4):414–421
114. Taylor GI (1941) The pressure and impulse of submarine explosion waves on plate. Cambridge University Press, Cambridge
115. Kennard EH (1941) Report on Underwater Explosions. David Taylor Model Basin Underwater Explosion (UNDEX) Research, Oct; Office of Naval Research (ONR, 1950)
116. Kambouchev N, Noels L, Radovitzky R (2006) Nonlinear compressibility effects in fluid–structure interaction and their implications on the air-blast loading of structures. J Appl Phys 100(6), Article Number: 063519
117. Kambouchev N, Radovitzky R, Noels L (2007) Fluid–structure interaction effects in the dynamic response of free-standing plates to uniform shock loading. J Appl Mech 74: 1042–1045
118. Dawson RL, Sullivan GM (1995) A theoretical investigation of the effect of structural stiffness in underwater shock wave loading using the plane wave approximation. J Appl Mech 62(1):260–262
119. Liu Z, Young YL (2008) Transient response of submerged plates subject to underwater shock loading: an analytical perspective. J Appl Mech 75(4), Article Number: 044504
120. Motley MR, Young YL. Liu Z (2011) Three-dimensional underwater shock response of composite marine structures. J Appl Mech 78(6), Article Number: 061013
121. Huang H (1969) Transient interaction of plane acoustic waves with a spherical elastic shell. J Acoust Soc Am 45(3):661–670
122. Huang H (1970) An exact analysis of the transient interaction of acoustic plane waves with a cylinder elastic shell. J Appl Mech 37:1091–1099
123. Huang H (1971) Early time interaction of spherical acoustic waves and a cylindrical shell. J Acoust Soc Am 50(3):885–891
124. Huang H, Wang YF (1971) Early-time interaction of spherical acoustic waves and a cylindrical elastic shell. J Acoust Soc Am 50(3B):885–891
125. Huang H, Lu YP, Wang YF (1974) Transient interaction of spherical acoustic waves, a cylindrical elastic shell, and its internal multidegree-of-freedom mechanical system. J Acoust Soc Am 56(1):4–10
126. Huang H (1975) Scattering of spherical pressure pulses by a hard cylinder. J Acoust Soc Am 58(2):310–317
127. Huang H (1979) Transient response of two fluid-coupled spherical elastic shells to an incident pressure pulse. J Acoust Soc Am 65(4):881–887
128. Huang H (1979) Transient response of two fluid-coupler cylindrical elastic shells to an incident pressure pulse. J Acoust Soc Am 46:513–518
129. Huang H, Gaunard GC (1998) Transient diffraction of a plane step pressure pulse by a hard sphere: neoclassical solution. J Acoust Soc Am 104(6):3236–3244
130. Huang H (1981) Interaction of acoustic shock waves with a cylindrical elastic shell immersed near a hard surface. Wave Motion 3(3):269–278
131. Payton RG (1960) Transient interaction of an acoustic wave with a circular cylindrical shell. J Acoust Soc Am 32:722–729
132. Tang SC, Yen DHY (1970) Interaction of a plane acoustic wave with an elastic spherical shell. J Acoust Soc Am 47(5):1325–1333
133. Lai WH (2007) Transient dynamic response of submerged sphere shell with an opening subjected to underwater explosion. Ocean Eng 34(5–6):653–664
134. Lam KY, Zhang ZJ, Gong SW, Chan ES (1998) The transient response of a two-layered elastic cylindrical shell impinged by an underwater shock wave. Compos Part B Eng 29(6):673–685
135. Lam KY, Zhang ZJ, Gong SW, Chan ES (1998) The transient response of submerged orthotropic cylindrical shells exposed to underwater shock. Compos Struct 43(3):179–193
136. Li J, Hua H (2009) Transient response of an orthotropic cylindrical shell to an underwater explosive loading. J Reinf Plast Comp 28(14):1747–1762
137. Li J, Hua H (2009) Transient interaction of a plane acoustic wave with an elastic orthotropic cylindrical shell. Thin-Walled Struct 47(3):335–345

138. Li J, Hua H (2009) Transient vibrations of laminated composite cylindrical shells exposed to underwater shock waves. Eng Struct 31(3):738–748
139. Hu G, Xia F, Li J (2010) The transient responses of two-layered cylindrical shells attacked by underwater explosive shock waves. Compos Struct 92(7):1551–1560
140. Hung CF, Hsu PY, Hwang-Fuu JJ (2005) Elastic shock response of an air-backed plate to underwater explosion. Int J Impact Eng 31(2):151–168
141. Hung CF, Lin BJ, Hwang-Fuu JJ, Hsu PY (2009) Dynamic response of cylindrical shell structures subjected to underwater explosion. Ocean Eng 36(8):564–577
142. Iakovlev S, Dooley G, Williston K, Gaudet J (2011) Evolution of the reflection and focusing patterns and stress states in two-fluid cylindrical shell systems subjected to an external shock wave. J Sound Vib 330(25):6254–6276
143. Iakovlev S, Gaudet J, Dooley G, MacDonald B (2010) Hydrodynamic fields induced by the shock response of a fluid-filled submerged cylindrical shell containing a rigid co-axial core. J Sound Vib 329(16):3359–3381
144. Iakovlev S, Mitchell M, Dooley G (2011) Modeling two-fluid response of thin elastic shells. Int J Num Methods Fluids 65(11–12):1389–1406
145. Iakovlev S (2009) Interaction between an external shock wave and a cylindrical shell filled with and submerged into different fluids. J Sound Vib 322:401–437
146. Iakovlev S (2008) Interaction between a submerged evacuated cylindrical shell and a shock wave – part I: diffraction-radiation analysis. J Fluids Struct 24:1077–1097
147. Iakovlev S (2008) Interaction between a submerged evacuated cylindrical shell and a shock wave-part II: numerical aspects of the solution. J Fluids Struct 24(7):1098–1119
148. Iakovlev S (2007) Radiation by a submerged cylindrical shell in response to an external non-stationary acoustic pulse. Can Acous Acoustique Canadienne 35(3):168–169
149. Iakovlev S (2007) Submerged fluid-filled cylindrical shell subjected to a shock wave: fluid–structure interaction effects. J Fluids Struct 23(1):117–142
150. Iakovlev S (2006) External shock loading on a submerged fluid-filled cylindrical shell. J Fluids Struct 22(8):997–1028
151. Iakovlev S (2004) Influence of a rigid coaxial core on the stress–strain state of a submerged fluid-filled circular cylindrical shell subjected to a shock wave. J Fluids Struct 19(7):957–984
152. Iakovlev S (2003) Interaction of a spherical shock wave and a submerged fluid-filled circular cylindrical shell. J Sound Vib 255(4):615–633
153. Iakovlev S (2002) Complex shock loading on submarine oil pipelines. Can Acous Acoustique Canadienne 30(3):88–89
154. Leblond C, Sigrist JF, Iakovlev S (2008) A semi-analytical approach to the study of the transient acoustic response of cylindrical shells. Can Acous Acoustique Canadienne 36(3):166–167
155. Leblond C, Iakovlev S. Sigrist JF (2010) A fully elastic model for studying submerged circular cylindrical shells subjected to a weak shock wave. Proceedings of the ASME pressure vessels and piping conference, Prague, Czech Republic, 26–30 July 2009, vol 4, pp 557–564
156. Leblond C, Iakovlev S, Sigrist JF (2009) A fully elastic model for studying submerged circular cylindrical shells subjected to a weak shock wave. Mecanique Industries 10(3–4):275–284
157. Leblond C, Sigrist JF (2010) A versatile approach to the study of the transient response of a submerged thin shell. J Sound Vib 329(1):56–71
158. Sigrist JF, Leblond C (2008) A semi-analytical approach for the modelling of acoustic shock wave-elastic submerged shell interaction. Application to the pre-design of submarine hulls. Mecanique Industries 9(6):543–550
159. Hasheminejad SM, Abbasion S, Mirzaei Y (2011) Acoustic pulse interaction with a submerged functionally graded material hollow cylinder. Acoust Phys 57(1):20–35
160. Hasheminejad SM, Bahari A, Abbasion S (2011) Modelling and simulation of acoustic pulse interaction with a fluid-filled hollow elastic sphere through numerical Laplace inversion. Appl Math Model 35(1):22–49
161. Hasheminejad SM, Abbasion S, Bahari A (2010) Time domain computation and visualization of shock induced sound fields for a doubly fluid-loaded hollow cylinder. Comput Struct 88(19–20):1077–1091

162. A-man Z, Wen-shan Y (2011) Yao XL NUMERICAL simulation of underwater contact explosion. Appl Ocean Res 34:10–20
163. Panahi B, Ghavanloo E, Daneshmand F (2011) Transient response of a submerged cylindrical foam core sandwich panel subjected to shock loading. Mater Des 32(5):2611–2620
164. Feuillade C (2004) Animations for visualizing and teaching acoustic impulse scattering from spheres. J Acoust Soc Am 115(5):1893–1904
165. Bailey MR, McAteer JA, Pishchalnikov YA, Hamilton MF, Colonius T (2006) Progress in lithotripsy research. Acous Today 2:18–29
166. Bailey MR, Khokhlova VA, Sapozhnikov OA et al (2003) Physical mechanisms of the therapeutic effect of ultrasound – (a review). Acoust Phys 49(4):369–388
167. Dahake G, Gracewski SM (1997) Finite difference predictions of P-SV wave propagation inside submerged solids. II. Effect of geometry. J Acoust Soc Am 102(4):2138–2145
168. Dahake G, Gracewski SM (1997) Finite difference predictions of P-SV wave propagation inside submerged solids. I. Liquid–solid interface conditions. J Acoust Soc Am 102(4): 2125–2137
169. Cleveland RO, Tello JS (2004) Effect of the diameter and the sound speed of a kidney stone on the acoustic field induced by shock waves. Acous Res 5(2):37–43
170. Cleveland RO, Sapozhnikov OA (2005) Modeling elastic wave propagation in kidney stones with application to shock wave lithotripsy. J Acoust Soc Am 118(4):2667–2676
171. Sapozhnikov OA, Maxwell AD, MacConaghy B et al (2007) A mechanistic analysis of stone fracture in lithotripsy. J Acoust Soc Am 121(2):1190–1202
172. Young PG (2003) An analytical model to predict the response of fluid-filled shells to impact – a model for blunt head impacts. J Sound Vib 267(5):1107–1126
173. Young PG (2002) A parametric study on the axisymmetric modes of vibration of multi-layered spherical shells with liquid cores of relevance to head impact modeling. J Sound Vib 256(4):665–680
174. Engin AE, Liu YK (1970) Axisymmetric response of a fluid-filled spherical shell in free vibrations. J Biomech 3(1):11–22
175. Engin AE (1969) Vibrations of fluid-filled spherical shells. J Acoust Soc Am 46(1B):186–190
176. Babbs CF (2005) Brain motion and deformation during closed head injury in the presence of cerebrospinal fluid. J Mech Med Biol 5(2):277–306
177. Babbs CF (2006) A new biomechanical head injury criterion. J Mech Med Biol 6(4):349–371
178. Engin AE (1969) The axisymmetric response of a fluid-filled spherical shell to a local radial impulse – a model for head injury. J Biomech 2(3):325–341
179. Kenner VH, Goldsmith W (1973) Impact on a simple physical model of the head. J Biomech 6(1):1–11
180. Kenner VH, Goldsmith W (1972) Dynamic loading of a fluid-filled spherical shell. Int J Mech Sci 14(9):557–568
181. Engin AE, Liu YK (1970) Axisymmetric response of a fluid-filled spherical shell in free vibrations. J Biomech 3(1):11–16
182. Taylor PA, Ford CC (2009) Simulation of blast-induced. Early-time intracranial wave physics leading to traumatic brain injury. J Biomech Eng (6) 061007, DOI 10.1115/1.3118765
183. Moore DF, Jerusalem A, Nyein M et al (2009) Computational biology – modeling of primary blast effects on the central nervous system. NeuroImage 47:T10–T20
184. Grujicic M, Bell WC, Pandurangan B et al (2010) Blast-wave impact-mitigation capability of polyurea when used as helmet suspension-pad material. Mater Des 31(9):4050–4065
185. Grujicic M, Bell WC, Pandurangan B et al (2011) Fluid/structure interaction computational investigation of blast-wave mitigation efficacy of the advanced combat helmet. J Mater Eng Perform 20(6):877–893
186. Nyein MK, Jason AM, Yu L et al (2010) In silico investigation of intracranial blast mitigation with relevance to military traumatic brain injury. Proc Natl Acad Sci USA 107(48): 20703–20708